

Oxygen levels regulate the co-evolution of non-terrigenous silica and organic matter in deep- to semi-deep waters during the Ediacaran–Cambrian transition

Hezheng Dong ^{a,b}, Dongsheng Zhou ^{a,b,*}, Yufei Liang ^{a,b}, Lei Huang ^{a,b}

^a Key Laboratory of Polar Geology and Marine Mineral Resources (China University of Geosciences, Beijing), Ministry of Education, Beijing 100083, China

^b School of Ocean Sciences, China University of Geosciences (Beijing), Beijing 100083, China

ARTICLE INFO

Editor: Bing Shen

Keywords:

Ediacaran–Cambrian transition
Hydrothermal fluids
Organic matter
Dilution effect
Non-terrigenous silica

ABSTRACT

During the Ediacaran–Cambrian (E–C) transition, marine black shales enriched in carbon (C) and silicon (Si) were widely deposited. However, the migration mechanism of Si in bathyal to abyssal zones remains unclear, and the key factors controlling the co-evolution of non-terrigenous silicon (NTS) and organic matter (OM) are still undefined. In this study, we focused on deep- to semi-deep water black shales in the upper Dengying Formation (Upper Sinian) and the lower Wangyinpu Formation (Lower Cambrian) of the Pukoucun section in northwestern Jiangxi Province, South China. Using an integrated approach that combines mineralogy, organic geochemistry, and element geochemistry, we investigated the factors controlling the co-evolution of the OM burial and NTS deposition in deep- to semi-deep water environments. The results suggest that the co-evolution of the OM and NTS in deep- to semi-deep water zones differs significantly from that in shallow-water environments. Hydrothermal fluids from the Jiangnan deep fault provided abundant hydrothermal Si, which diffused from hydrothermal vents into broader areas in the form of Fe(II)-silicate gels. In addition, the redox proxies (Mo_{EF} , UEF , $\text{C}_{\text{org}}/\text{P}$, Ni/Co) show an increasing trend from the late Ediacaran to the early Cambrian, indicating that oxygen levels during this period exhibited an overall decreasing trend, accompanied by periodic fluctuations. Based on the co-variation relationships among Si_{ex} , TOC, Eu/Eu^* , and Fe/Al , it can be concluded that aqueous oxygen levels was the key controlling factor for the co-evolution of OM and NTS in deep- to semi-deep water settings along the southeastern margin of the Yangtze Platform during the E–C transition. We propose a new model of the co-evolution process, in which the extent of the marine dynamic anoxia zone influences the migration distance of Fe(II)-silicate gels, thereby regulating the sedimentation flux of NTS in distal vent areas. Based on these observations, NTS is predominantly removed from seawater in an inorganic form, and its enrichment may dilute the concentration of OM. These findings enhance our understanding of how marine redox evolution influenced the C–Si cycle during the E–C transition and provide novel insights into shale OM enrichment mechanisms.

1. Introduction

The Lower Cambrian marine black shale represents one of the most important hydrocarbon source rock intervals globally (Craig, 2009). In the Yangtze region of South China, the Lower Cambrian Wangyinpu Formation—also referred to as the Niutitang, Shuijingtuo, or Hetang Formation in certain areas—is a typical representative. This formation is characterized by high organic carbon content, elevated silica levels, advanced thermal maturity, stable regional distribution, and considerable single-layer thickness (Zhang et al., 2022a, 2022b; Guo et al.,

2025). However, the underlying Late Ediacaran Dengying Formation (also known as the Liuchapo Formation or Piyuancun Formation) commonly exhibits a high-silica, low-carbon characteristic, which is exemplified by the widespread distribution of cherts and siliceous shales (Gao et al., 2020a, 2020b; Li et al., 2022a, 2022b). This abrupt shift in the OM abundance implies that there was a significant transformation in the marine environmental conditions during the E–C transition. Previous studies have indicated that high marine primary productivity is generally a prerequisite for OM enrichment of the black shales of the Lower Cambrian Wangyinpu Formation. Additionally, euxinic

* Corresponding author at: Key Laboratory of Polar Geology and Marine Mineral Resources (China University of Geosciences, Beijing), Ministry of Education, Beijing 100083, China.

E-mail address: dszhou@cugb.edu.cn (D. Zhou).

conditions play a crucial role in the preservation of OM (Li et al., 2015; Wu et al., 2020a, 2020b; Zhou et al., 2024). Notably, non-terrigenous silica (NTS) is significantly enriched during the deposition of OM-rich layers. NTS may dilute OM by increasing the sediment flux, and in some cases, it may even become a key factor influencing the OM abundance of black shales (Chu et al., 2016; Zhou et al., 2024; Dong et al., 2025).

Throughout the Earth's history, the concentration of dissolved Si (H_4SiO_4 , DSi) in seawater has decreased progressively, from over 1000 $\mu\text{mol/L}$ during the Precambrian to the present-day global average of approximately 70 $\mu\text{mol/L}$ (Conley et al., 2017). Despite this overall decreasing trend, NTS enrichment of Archean to Cenozoic marine sediments has been commonly observed (Beauchamp and Baud, 2002; Wang et al., 2009; Marin-Carbonne et al., 2014; Gao et al., 2020a, 2020b; Jurkowska and Świerczewska-Gładysz, 2020). The principal external sources of Si to the ocean are dominated by continental weathering and hydrothermal activity (Tréguer et al., 2021). After undergoing a complex biogeochemical cycle, DSi is ultimately buried in marine sediments, forming a long-term Si sink. In contrast to the modern ocean, in which biological silicification dominates, the Precambrian oceans were largely devoid of abundant silica-secreting organisms (Conley et al., 2017; Tatzel et al., 2017). As a result, alternative mechanisms such as hydrothermal Si deposition (Isley, 1995) and replacement of carbonate rocks (Maliva et al., 2005) played a more significant role in silica enrichment during that period. During the E–C transition, the global ocean underwent episodes of oceanic oxygenation (Lyons et al., 2014). This environmental change coincided with the rapid diversification of metazoans, an event commonly referred to as the Cambrian Explosion (Amthor et al., 2003; Steiner et al., 2007). This evolutionary radiation was accompanied by a marked increase in the abundance of siliceous sponges and other silica-secreting organisms. Consequently, biogenic silica became an increasingly important pathway for the removal of marine DSi (Conley et al., 2017), marking a key shift in the global Si cycle that was linked to both environmental and evolutionary changes.

Currently, it is widely accepted that biogenic silica was the dominant source of the NTS in the shallow-water black shales of the Yangtze Platform during the E–C transition (Zhang et al., 2023; Zhou et al., 2024). In these shallow-water settings, OM and NTS often exhibit synchronous variations, with no significant dilution effects (consistent with biogenic silica as the dominant source of NTS). In contrast, deep- and semi-deep water environments are generally considered to be dominated by inorganic Si deposition, and NTS enrichment is primarily controlled by hydrothermal activity (Zhang et al., 2017; Xie et al., 2021; Zhou et al., 2024). Under such conditions, an increase in the sediment flux may lead to the dilution of OM. The difference in the silicification mechanisms in these two depositional settings results in distinct NTS–OM co-variation patterns. This spatial heterogeneity has two key implications. First, it suggests that under the broader macro-oxidation background (i.e., progressive ocean oxygenation), biological evolution in shallow-water areas outpaced that in deeper environments. Second, it indicates that the dynamic balance between NTS and OM accumulation in deep- and semi-deep water areas may reflect coupling of the marine Si and carbon (C) cycles.

Although previous studies have generally linked the deposition of inorganic Si to hydrothermal fluid activity in deep- to semi-deep water marine settings (Zhang et al., 2017; Xie et al., 2021; Zhou et al., 2024), the specific mechanisms of NTS enrichment, such as the migration and deposition of Si following hydrothermal input, remain poorly constrained. In particular, the spatial distribution and enrichment processes of NTS in regions surrounding hydrothermal vents (on a broader scale) remain unclear. Si is generally considered to be a non-redox-sensitive element; however, its biogeochemical cycling may be indirectly modulated by changes in oceanic redox conditions (Reddy et al., 2016; Zheng et al., 2016; Li et al., 2022a, 2022b; Tostevin and Sevgen, 2024). Therefore, during the E–C transition, when the global ocean experienced

significant redox fluctuations, including episodes of expanded dynamic anoxia, these changes likely impacted not only the enrichment of OM but also the accumulation of NTS by altering the efficiency of Si transport and transformation. This raises an important question: did the oxygen level of the water column act as a key factor regulating the dynamic balance between NTS and OM in deep- and semi-deep water settings?

In view of the above-mentioned issues, in this study, we focused on the Pukoucun (PKC) section in the Xiuwu Basin, South China. The target intervals consist of the C-rich, Si-rich black shales of the upper member of the Dengying Formation and the lower member of the Wangyinpu Formation, which were deposited continuously during the E–C transition. These strata preserve critical records of changes in the marine environment during this pivotal period. Based on paleo-oceanographic reconstruction, in this study, we systematically investigated the mechanisms underlying NTS enrichment in deep- and semi-deep water settings, with the aim of identifying the key factors that regulate the dynamic balance between NTS and OM. The results of this study provide a better understanding of how fluctuations in marine redox conditions modulated the coupling of the C and Si cycles during the E–C transition, as well as information for refining the theoretical framework of OM enrichment in black shales.

2. Geologic setting

During the Late Neoproterozoic, the accelerated breakup of the Rodinia supercontinent (Veevers et al., 1997) triggered the development of an intracontinental rift within the South China Block (Zheng et al., 2008). Subsequently, as the extensional tectonic activity intensified, the Yangtze Platform gradually rifted apart from the Cathaysian Platform, leading to progressive opening of the Nanhua Basin. This tectonic evolution facilitated the formation of a broad shelf along the southeastern margin of the Yangtze Platform, which eventually evolved into a passive continental margin (Wang, 2003). During the E–C transition, the South China landmass drifted toward lower latitudes (Fig. 1a). As a major component of this landmass, the Yangtze Platform preserved a continuous sedimentary succession spanning shallow- to deep-water environments owing to its relatively stable tectonic framework (Jiang et al., 2011; Wang et al., 2020; Chang et al., 2022). This makes the region an ideal natural laboratory for investigating the evolution of the marine environment during this critical transitional period. At that time, the Yangtze Platform exhibited a paleogeographic pattern characterized by alternating uplift and subsidence, commonly referred to as a “platform sandwiched between two basins” configuration (Fig. 1b). In addition, the study area is traversed by a major deep fault—the Jiangnan deep fault. This long-lived, cryptic fault zone significantly influenced the geological evolution of southern China and its adjacent regions from the Proterozoic to the Early Paleozoic, and it may be a crustal suture zone (Yang, 1981). The PKC section is located on its southern side (Fig. 2). During the Early Paleozoic, the Jiangnan deep fault controlled the subsidence along the margin of the Yangtze Platform and served as a key sedimentary facies transition zone. Abrupt differences in the sedimentary strata and paleontological assemblages have been observed across the fault (Yang, 1981). In addition, extensional tectonics may have reactivated the Jiangnan deep fault, and magmatic emplacement could have initiated geothermal circulation of the surrounding groundwater (Steiner et al., 2001; Han et al., 2015; Dong et al., 2025). During the Early Cambrian, a large-scale transgression inundated the platform, resulting in widespread marine sedimentation. The sedimentary environments transitioned gradually from northwest to southeast, encompassing carbonate platform facies, continental shelf facies, slope facies, and deep-water basin facies—thus forming a complete deep-marine depositional sequence (Wang et al., 1985; Lehmann, 2022). The key sedimentary records in the region include the upper Ediacaran Dengying Formation (also referred to as the Liuchapo, Piyuancun, or Laobao Formation in different areas), which is conformably overlain by the Lower Cambrian Wangyinpu Formation. The E–C boundary (538.8 ±

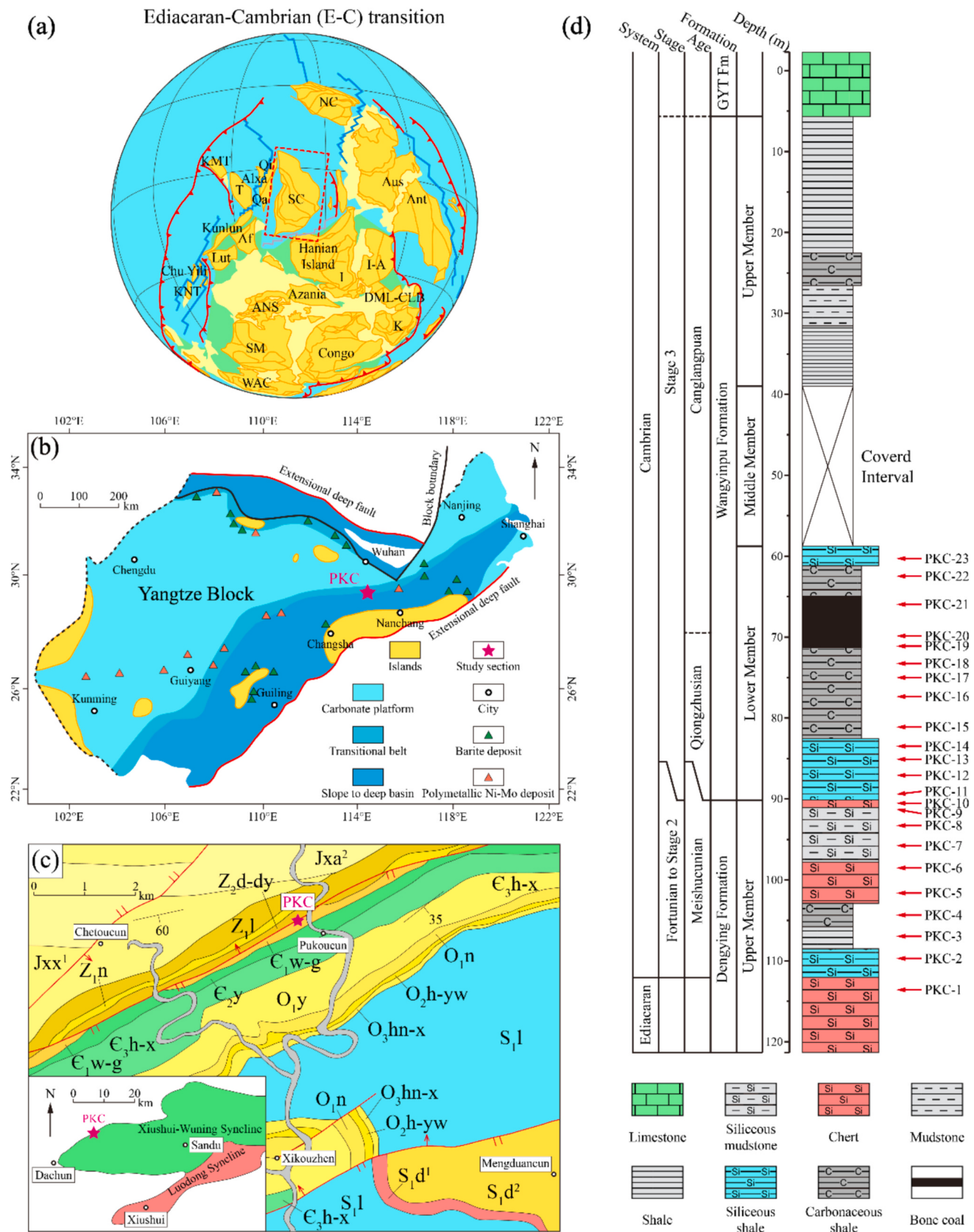


Fig. 1. (a) Paleo-plate tectonic model during the E-C transition (modified from Merdith et al., 2021); (b) Simplified map showing the paleogeography of the Yangtze Platform during the E-C transition (modified from Wang et al., 1985; Lehmann, 2022); (c) The 1:200000 geological map of the study area (source from China Geological Survey); (d) Lithologic columns of the Lower Cambrian Wangyinpu Formation and Upper Ediacaran Dengying Formation from the PKC section in the northwest Jiangxi Province, Lower Yangtze area. The red arrow represents the sampling point. MSC = Meishucunian Age; QZS = Qiongzhusian Age; GYT Fm = Guanyintang Formation. (For interpretation of the references to colour in this figure legend, the reader is referred to the web version of this article.)

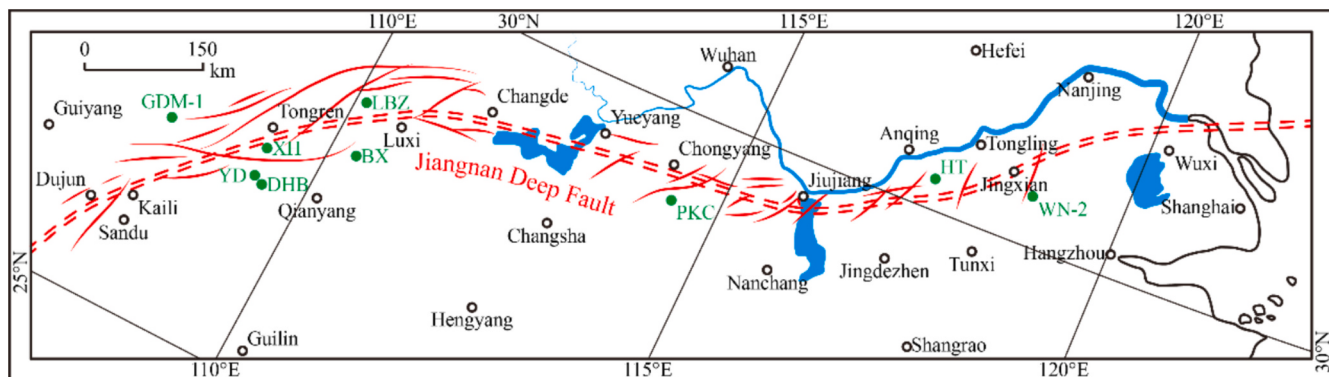


Fig. 2. Map showing the location of hyalophane discoveries in the Lower Cambrian Wangyinpu Formation in relation to the Jiangnan deep fault. The base map is adapted from Yang (1981), with data points compiled from Wu (2000); Han et al. (2015); Huang et al. (2018); Chang et al. (2018); Wu et al. (2020a, 2020b); Liu et al. (2023); and Dong et al. (2025).

0.6 Ma) is generally placed at the top of the Dengying Formation.

The study area is located in the Xiuwu Basin, which is part of the Lower Yangtze Platform. This basin comprises two secondary tectonic units: the Xiushui-Wuning syncline and the Luodong syncline. The PKC section selected for analysis in this study is located in the western margin of the Xiushui-Wuning syncline ($114^{\circ}23'12''E$, $29^{\circ}12'22''N$) (Fig. 1c). Previous geological surveys have confirmed that the PKC section consists of a complete exposed stratigraphic succession of the Upper Sinian Dengying Formation and the Lower Cambrian Wangyinpu Formation. These two units are conformably overlain, and there is no significant discontinuity between them (Fig. 1c). Thus, this section provides a continuous sedimentary record for reconstructing the evolution of the depositional environment during the E-C transition.

From a regional paleogeographic perspective, the study area was situated in a slope to deep-basin environment during the E-C transition and was bounded by the Yangtze Platform and the Jiangnan paleo-uplift (a submarine highland) (Fig. 1b). This paleogeographic setting was characterized by limited terrigenous input and a relatively restricted water column, which is highly consistent with the sedimentary conditions of the deep- and semi-deep water areas described earlier. In terms of the lithostratigraphic characteristics, the upper part of the Dengying Formation in the study area (encompassing Tongshan in Hubei Province and Xiushui in Jiangxi Province) exhibits lateral lithofacies variations, transitioning gradually from chert interbedded with carbonaceous siliceous shale to dolomite-dominated sediment. This lateral transition reflects the differentiation of the depositional environments. The overlying Wangyinpu Formation was conformably deposited on the Dengying Formation, and OM-rich black shales are widely developed in the lower part of the Wangyinpu Formation. Locally, high OM enrichment has led to the formation of bone coal (Wei et al., 1984; Huang et al., 1990). As shown in the stratigraphic column of the PKC section (Fig. 1d), the upper member of the Dengying Formation is dominated by chert and siliceous mudstones interbedded with thin layers of carbonaceous siliceous shales. The base of the lower member of the Wangyinpu Formation consists of a siliceous shale unit, which gradually transitions upward into carbonaceous shale and local occurrences of bone coal seam. The middle member is covered by vegetation and regolith, while the upper member is characterized by gray-green shale. This lithological succession not only records the depositional processes of the NTS and OM but also potentially reflects the changes in the sedimentary environment, such as variations in the redox conditions.

3. Materials and methods

3.1. Samples

In this study, a total of 23 samples were systematically collected from

the target intervals of the PKC section in the Lower Yangtze Platform in northwest Jiangxi Province. These samples include 10 samples from the Upper Sinian Dengying Formation and 13 samples from the Lower Cambrian Wangyinpu Formation. The sampling positions correspond to key horizons within the lithostratigraphic sequence (Fig. 1d), enabling comprehensive coverage of the main depositional stages of the siliceous material and OM during the E-C transition. To address the research objectives, multidisciplinary geochemical and microscopic analyses were conducted on all of the samples. These analyses included total organic carbon (TOC) determination, as well as major, trace, and rare earth element (REE) geochemical analyses. In addition, selected samples were examined using field emission scanning electron microscopy (FE-SEM) to characterize the mineralogical and microstructural features.

3.2. Methods

3.2.1. Total organic carbon analysis

The TOC analysis was conducted at the Geological Experimental Research Center of the Research Institute of Petroleum Exploration and Development, PetroChina, Beijing, China. The analytical procedure was as follows: each sample was crushed and ground in an agate mortar to a particle size of less than 200 mesh to avoid metal contamination, which could affect the accuracy of the TOC measurements. Approximately 0.0500 g of the powdered sample was then treated with 10 % hydrochloric acid (HCl) to remove any carbonate minerals, which can interfere with the organic carbon determination. The residue was repeatedly washed with distilled water until a neutral pH was achieved, ensuring complete removal of the residual HCl. Following drying, the TOC content was measured using an Elementrac CS-i carbon and sulfur analyzer. Based on replicate analyses and quality control procedures specified in Chinese national standard GB/T 19145–2003 (Zeng et al., 2013), the instrumental precision is within $\pm 0.5\%$ of the reported TOC values.

3.2.2. Major, trace, and rare earth element analyses

The major, trace, and REE analyses were conducted at the Geological Experiment Research Center of the Research Institute of Petroleum Exploration and Development, PetroChina. The experimental procedures and quality control measures were as follows: approximately 1200 mg of powdered sample were weighed and oxidized at $900^{\circ}C$ for 3 h to remove the OM and sulfides. Subsequently, the oxidized sample was mixed with lithium tetraborate ($Li_2B_4O_7$) at a mass ratio of 1:8 and fused at approximately $1200^{\circ}C$ to form a homogeneous glass bead. The major oxide contents of the samples were then determined using a M4 TORNADO X-ray fluorescence (XRF) spectrometer.

The trace and REE concentrations were analyzed using an inductively coupled plasma mass spectrometer (ICP-MS; Thermo Scientific Element XR) at the same laboratory. The analytical procedure was as

follows: approximately 50 mg of powdered sample was weighed into a Teflon bomb and moistened with a few drops of ultrapure water. Then, 1 mL each of concentrated HNO_3 and HF was added. The bomb was sealed and heated in an oven at 190 °C for over 48 h to ensure complete dissolution of the sample. After cooling, the bomb was carefully opened, and the solution was evaporated to near dryness on a hot plate at 115 °C. Subsequently, 1 mL of concentrated HNO_3 was added, and the residue was re-evaporated to remove the fluoride ions. The resulting residue was then redissolved in 3 mL of 30 % HNO_3 , resealed, and heated at 190 °C for 12 h under a nitrogen atmosphere to ensure full digestion. Finally, the digested solution was transferred to a polyethylene bottle and diluted to approximately 100 g with a 2 % HNO_3 solution, corresponding to a dilution factor of ~2000. The prepared solutions were then analyzed via ICP-MS. The analytical precision and accuracy were monitored via triplicate measurements of selected samples and the analysis of three international reference materials, namely, BCR-2 (basalt), BHVO-2 (basaltic glass), and GSR-6 (granite). For most of the trace elements, the analytical precision is better than ±5 %, as reported in the replicate analyses (Liu et al., 2017).

3.2.3. FE-SEM observations

The FE-SEM observations were conducted at the Petroleum Geology Experimental Research Center, Research Institute of Petroleum Exploration and Development, PetroChina. A high-resolution field emission scanning electron microscope (FEG 450/X Flash Detector 5030) was used to conduct the observations. This instrument was equipped with an energy-dispersive X-ray spectrometer (EDS) for element analysis. To obtain a highly polished, smooth surface suitable for high-resolution imaging, the samples were subjected to argon ion milling using an IM4000 system prior to the FE-SEM analysis. The FE-SEM imaging was performed at a working distance of 3.9–4.0 mm and an accelerating voltage of 5 kV. For the mineralogical identification, selected areas were analyzed in backscattered electron (BSE) mode via EDS, with a working distance of 4.0 mm and an accelerating voltage of 10 kV.

3.3. Proxy calculations

Aluminosilicate minerals are the primary source of aluminum (Al) in sediments, and they remain relatively stable during diagenesis (Piper and Perkins, 2004). For this reason, element concentrations (X) are commonly normalized to Al (expressed as X/Al) to account for variations in the sediment composition. Given that the proportion of aluminosilicates in the sediment matrix is relatively consistent across different lithologies, Al normalization helps correct for dilution effects induced by differences in the grain size and non-aluminosilicate components among samples. This normalization approach effectively minimizes the influence of lithological variability on element concentrations and reduces potential biases arising from heterogeneity of the sediments (Calvert and Pedersen, 1993; Van Der Weijden, 2002; Tribouillard et al., 2006).

Element enrichment factors (EFs) are often used to quantify the degrees of enrichment or depletion of elements (e.g., Mo and U) and provide valuable insights into the origin, migration, and sedimentation processes of elements in different geological settings (Calvert and Pedersen, 1993; Tribouillard et al., 2006). The element EF can be calculated using the following formula:

$$X_{\text{EF}} = (X/\text{Al})_{\text{sample}} / (X/\text{Al})_{\text{PAAS}} \quad (1)$$

where X_{EF} is the enrichment factor of element X; X_{sample} and $\text{Al}_{\text{sample}}$ are the concentrations of element X and Al in the sample, respectively; and X_{PAAS} and Al_{PAAS} are the concentrations of element X and Al in post-Archean Australian average shale (PAAS), respectively (Taylor and McLennan, 1985).

To estimate the non-terrigenous input component of a given element (X), the terrigenous detrital contribution must be subtracted from the total concentration of X. Al, as an element predominantly from terrig-

enous detritus (Holdaway and Clayton, 1982; Liu et al., 2017), is commonly used to subtract the terrigenous input component. The calculation formula is as follows:

$$X_{\text{ex}} = X_{\text{sample}} - (\text{Al}_{\text{sample}} \times (X/\text{Al})_{\text{PAAS}}) \quad (2)$$

where X_{ex} is the non-terrigenous input component of X. X_{sample} and $\text{Al}_{\text{sample}}$ are the concentrations of element X and Al in the sample, respectively; and X_{PAAS} and Al_{PAAS} are the concentrations of element X and Al in PAAS (Taylor and McLennan, 1985), respectively. Specifically, in this study, $(\text{Si}/\text{Al})_{\text{PAAS}}$ was set to 2.93, and thus, the excess Si (Si_{ex}) calculated using this formula was interpreted to be NTS.

The europium anomaly (Eu/Eu^*) and cerium anomaly (Ce/Ce^*) are key indicators for reconstructing the paleo-marine sedimentary environment (Gao et al., 2020a, 2020b; Zhu et al., 2021). They can be calculated using the following formulas:

$$\text{Eu}/\text{Eu}^* = 2\text{Eu}_{\text{N}} / (\text{Sm}_{\text{N}} + \text{Gd}_{\text{N}}) \quad (3)$$

$$\text{Ce}/\text{Ce}^* = 2\text{Ce}_{\text{N}} / (\text{La}_{\text{N}} + \text{Pr}_{\text{N}}) \quad (4)$$

where Eu_{N} , Sm_{N} , Gd_{N} , Ce_{N} , La_{N} , and Pr_{N} are the normalized values of Eu, Sm, Gd, Ce, La, and Pr in the sample, respectively, using the corresponding PAAS values for normalization.

The chemical index of alteration (CIA), first proposed by Nesbitt and Young (1982), is calculated as follows:

$$\text{CIA} = \text{Al}_2\text{O}_3 / (\text{Al}_2\text{O}_3 + \text{CaO}^* + \text{Na}_2\text{O} + \text{K}_2\text{O}) \times 100 \quad (5)$$

where CaO^* is the CaO content of the silicate fraction. CaO^* is calculated using the method proposed by McLennan (1993). The specific formula is as follows:

$$\text{CaO}^* = \min (\text{CaO} - 10/3 \times \text{P}_2\text{O}_5, \text{Na}_2\text{O}) \quad (6)$$

The sulfate reduction index (SRI) can be used to characterize the intensity of bacterial sulfate reduction (BSR) (Lallier-Vergès et al., 1993; Liu et al., 2021). It can be calculated using the following simple formula:

$$\text{SRI} = 1 + 0.75 \times \text{TS/TOC} \quad (7)$$

The SRI is based on the assumption that all of the hydrogen sulfide produced is either precipitated as sulfides in the sediments or is incorporated into organic compounds. For this reason, the SRI should be regarded as the minimum index of the degradation of TOC, reflecting the extent of the OM depletion induced by BSR (Liu et al., 2021).

4. Results

4.1. Toc

The TOC contents of the studied samples range from 0.08 % to 17.0 %, with an average of 3.37 %. Table S1 presents the specific data; and the vertical distribution characteristics are shown in Fig. 3a. In terms of the stratigraphic sequence, the TOC contents of the lower Wangyinpu Formation are significantly higher than those of the upper Dengying Formation: the former range from 0.18 % to 17.0 % (average 5.25 %), while the latter range from 0.08 % to 4.40 % (average of 0.98 %). This difference is closely associated with lithologic background—the upper member of the Dengying Formation is dominated by chert, siliceous mudstone, and siliceous shale. The lower member of the Wangyinpu Formation exhibits more distinct variations in the TOC content due to the occurrence of lithological differentiation (Fig. 3a): the TOC contents of the basal siliceous shales range from 0.14 to 1.70 % (average of 0.64 %), which is consistent with the siliceous sedimentary characteristics of the upper member of the Dengying Formation (silica-dominated lithology with low TOC). After transitioning upward to carbonaceous shale, the TOC content increases significantly (0.26–17.0 %, average of 8.07 %) with an expanded fluctuation range. Due to the high OM enrichment, the TOC contents of the intercalated stone coal seams reach 12.5–17.0 %

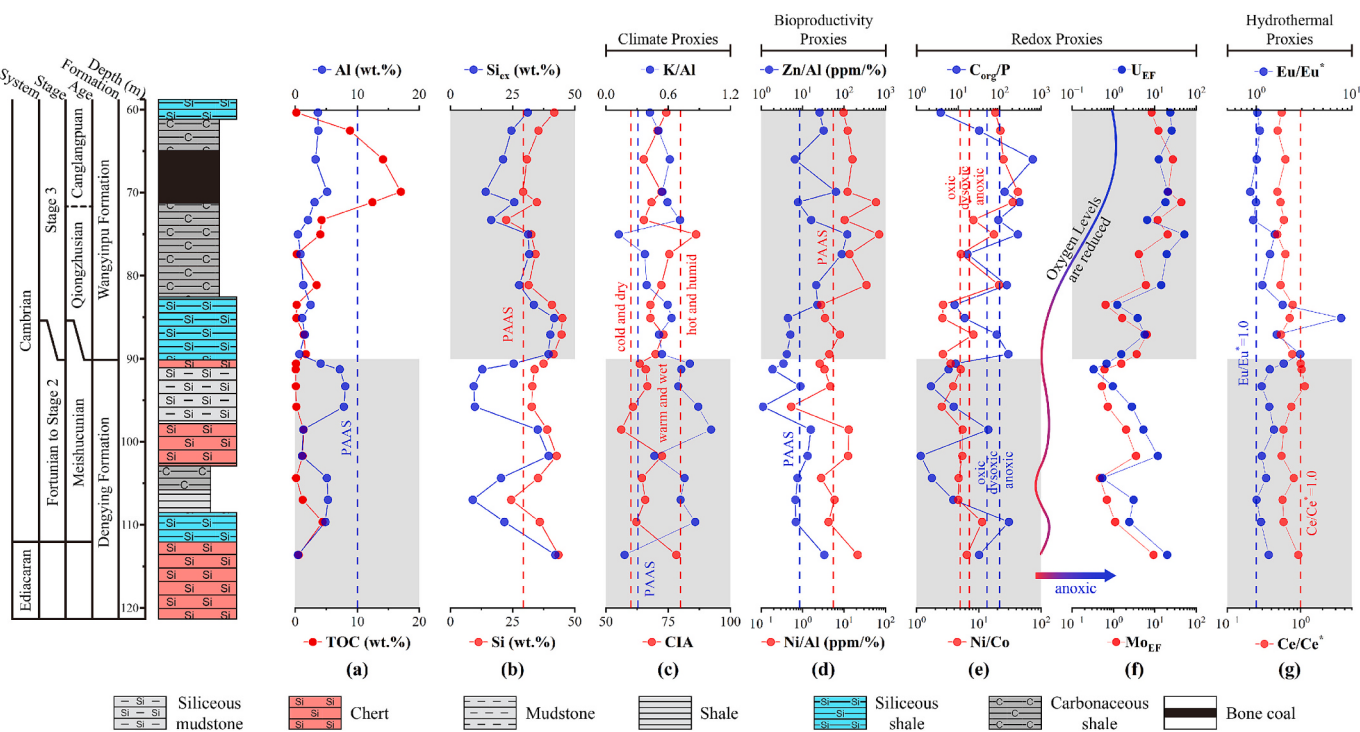


Fig. 3. Vertical variations of multiple geochemical proxies in the Lower Cambrian Wangyinpu Formation and Upper Ediacaran Dengying Formation at the PKC section. For CIA, the ranges are: cold and dry 50–60, warm and wet 60–80, hot and humid 80–100 (Fedo et al., 1995). For C_{org}/P, the ranges are: oxic<50, dysoxic 50–100, anoxic>1.25 (Algeo and Ingall, 2007). For Ni/Co, the ranges are: oxic<5, dysoxic 5–7, anoxic>7 (Jones and Manning, 1994). The variation range is divided by corresponding colored dashed lines.

(average of 14.6 %), exhibiting abnormally high values.

4.2. Mineralogy

Representative samples from the PKC section were analyzed using FE-SEM. The results reveal that quartz is the dominant mineral in all of the lithologies. However, no biogenic siliceous aggregates (e.g., siliceous shells or skeletal fragments) were observed. In contrast, barium (Ba)-rich potassium feldspar (zonal hyalophane) is widely distributed across all the lithological types (Fig. 4). The following descriptions integrate the mineralogical and textural characteristics of selected representative samples. Siliceous shale sample (PKC-2, TOC = 4.40 %): FE-SEM observations revealed the occurrence of abundant well-preserved frambooidal pyrite (Fig. 4a). The OM primarily occurs as interstitial and massive forms and is closely associated with siliceous minerals via interbedding or envelopment. Additionally, numerous zoned hyalophane crystals with well-developed morphologies are present (Figs. 4a–c). Chert sample (PKC-10, TOC = 0.14 %): This sample also contains abundant zonal hyalophane (Figs. 4d–f), along with interstitial OM and locally occurring massive barite. Carbonaceous shale sample (PKC-20, TOC = 17.0 %): Microscopic observations revealed the presence of pyrite moldic pores (Fig. 4g). The OM occurs in both massive and interstitial forms. The sample is rich in clay minerals (Figs. 4g–i) and contains minor amounts of zonal hyalophane and massive barite (Fig. 4h). Compared to the chert and siliceous shale samples, the carbonaceous shale has a lower abundance of hyalophane. These mineralogical and textural features provide insights into the depositional and diagenetic processes that influenced the accumulation of silica and OM in the strata deposited during the E–C transition.

4.3. Element geochemistry

4.3.1. Major elements

The Al and Si contents of the upper Member of the Dengying

Formation and the lower Member of the Wangyinpu Formation are significantly different. Table S1 presents the specific data; and Fig. 3a and Fig. 3b show the distribution characteristics. The Al contents of the studied samples range from 0.43 % to 8.04 (average of 3.24 %), which are lower than the Al_{PAAS} value (10.0 %) (Taylor and McLennan, 1985) overall. In terms of the stratigraphic correlation, the Al contents of the upper member of the Dengying Formation are 0.43–8.04 % (average of 4.97 %), which are significantly higher than those of the lower member of the Wangyinpu Formation (0.44–5.13 %, average of 2.26 %) and exhibit a larger fluctuation range. Specifically, the carbonaceous shales in the upper member of the Dengying Formation have a relatively high proportion of clay minerals, with Al contents of 4.85–8.04 % (average of 6.37 %). The Si contents of the samples range from 22.4 % to 45.0 % (average of 35.7 %), which are higher than the Si_{PAAS} value (29.3 %) (Taylor and McLennan, 1985) overall (Table S1 and Fig. 3b). According to the lithological differences, the Si contents of the cherts and siliceous shales are higher than those of the carbonaceous shales. This is consistent with the mineralogical observations conducted via FE-SEM, that is, quartz is the dominant mineral, further confirming the enrichment of NTS in these lithologies.

The stratigraphic correlation reveals that the Si contents of the upper member of the Dengying Formation are 24.4–43.5 % (average of 34.9 %), which are comparable to those of the lower member of the Wangyinpu Formation (22.4–45.0 %, average of 35.7 %) overall. However, there are differences in the element covariation patterns of the two members. For the upper Dengying Formation, the Si content is negatively correlated with the Al content (Figs. 3a and b); while for the lower Wangyinpu Formation, the variations in Si content are mainly lithology-dependent, that is, the Si content of the siliceous shale is significantly higher than that of the carbonaceous shale, and the Si content exhibits a negative correlation with the TOC content (Figs. 3a and b). To characterize the enrichment of NTS more precisely, in this study, we calculated the excess silicon (Si_{ex}). The Si_{ex} contents range from 9.00 to 42.2 % (average of 26.2 %) (Table S1 and Fig. 3b). Similar to the total Si

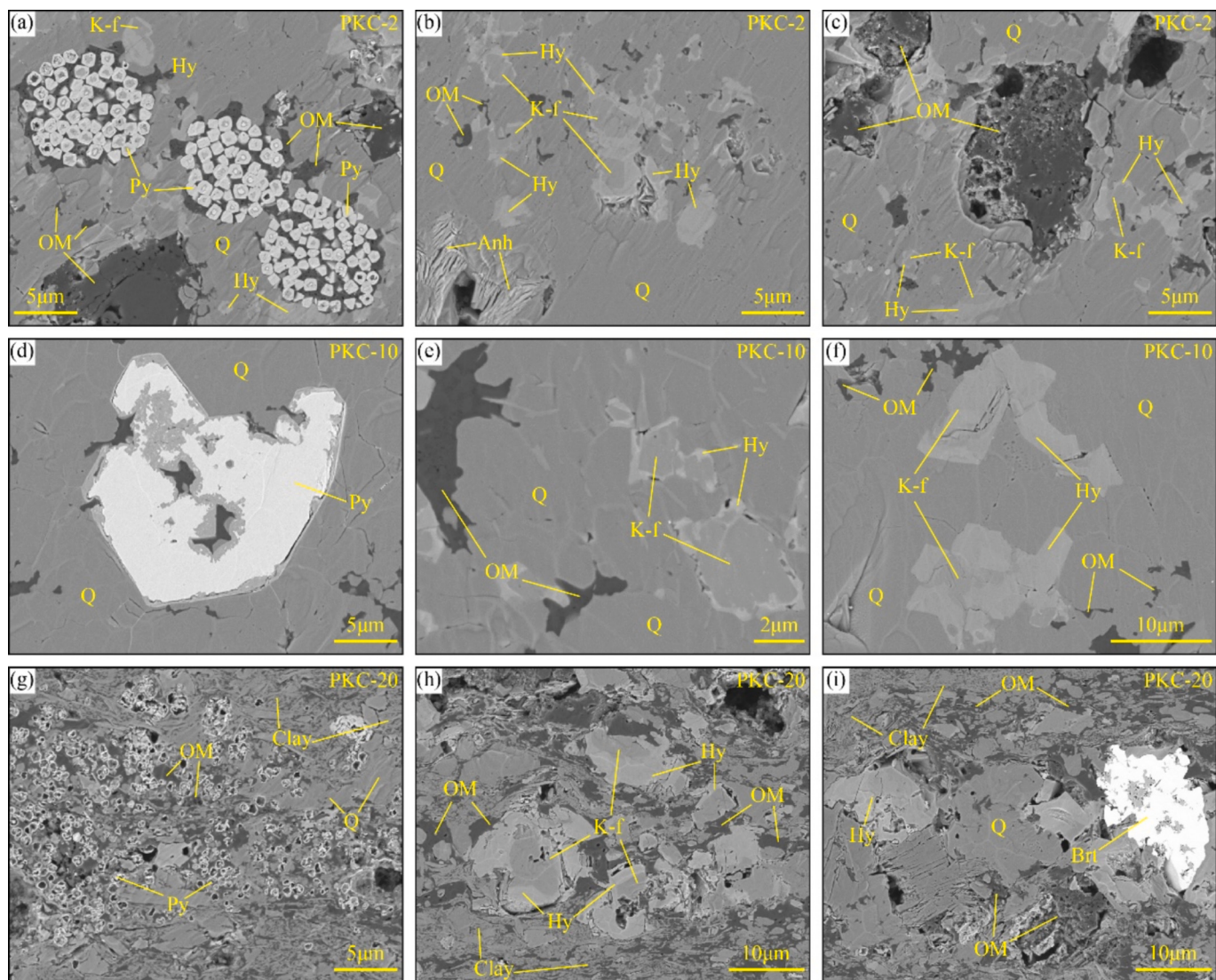


Fig. 4. FE-SEM images of the representative samples from the Dengying Formation and Wangyinpu Formation in the PKC section. (a) (b) (c) Aggregates of framboid pyrites with diameters of 1–2 μm , massive and interstitial OM, and zonal hyalophanes (sample PKC-2); (d) (e) (f) Massive pyrite, massive and interstitial OM, and zonal hyalophanes (sample PKC-10); (g) (h) (i) Aggregates of framboid pyrites with diameters of 1–2 μm , massive OM and OM mixed quartz and clay minerals, and massive barite (sample PKC-20). OM = organic matter; Q = quartz; K-f = K-feldspar; Py = pyrite; Hy = hyalophane; Anh = anhydrite; Brt = barite.

content, the Si_{ex} contents of the chert and siliceous shale are higher than those in carbonaceous shale. The vertical variation trend of the Si_{ex} is generally consistent with that of the total Si, but the fluctuation range of the Si_{ex} in the upper member of the Dengying Formation is larger (Fig. 3b).

4.3.2. Trace elements

To eliminate the interference of varying terrigenous input on the trace elements, the zinc (Zn) and nickel (Ni) contents were normalized by Al (i.e., Zn/Al and Ni/Al ratios). The Zn/Al ratios of the samples range from 1.10 ppm/% to 120 ppm/% (average of 22.4 ppm/%), and the Ni/Al values range from 0.53 ppm/% to 69.8 ppm/% (average of 14.2 ppm/%). Vertically, both ratios initially decrease and then increase (Fig. 3d). Table S1 presents the specific data. The stratigraphic correlation reveals that the Zn/Al ratios of the lower Wangyinpu Formation range from 4.16 ppm/% to 120 ppm/% (average of 31.5 ppm/%), and the Ni/Al values range from 2.79 ppm/% to 69.8 ppm/% (average of 19.7 ppm/%), both of which are significantly higher than those of the upper member of the Dengying group (Zn/Al: 1.10–33.2 ppm/%, average of 7.24 ppm/%; Ni/Al: 0.53–21.3 ppm/%, average of 5.49 ppm/%).

%). Further comparison to PAAS reveals that the Zn/Al and Ni/Al ratios of the lower Wangyinpu Formation are generally higher than the PAAS standard values ($\text{Zn}/\text{Al}_{\text{PAAS}} = 8.5 \text{ ppm}/\%$, $\text{Ni}/\text{Al}_{\text{PAAS}} = 5.5 \text{ ppm}/\%$) (Taylor and McLennan, 1985), whereas those of the upper Dengying Formation are close to the PAAS values overall.

The ratios of several trace elements, including $\text{C}_{\text{org}}/\text{P}$ (1.26–630, average of 95.5) and Ni/Co (2.54–42.4, average of 11.5), also exhibit a similar trend of increasing from bottom to top (Table S1 and Fig. 3e). Specifically, the $\text{C}_{\text{org}}/\text{P}$ (3.80–630, mean of 147) and Ni/Co (2.60–42.4, mean of 16.2) ratios of the lower member of the Wangyinpu Formation are significantly higher than those of the upper member of the Dengying Formation ($\text{C}_{\text{org}}/\text{P}$: 1.26–167, mean of 28.5; Ni/Co: 2.54–11.3, mean of 5.17).

Geochemically, the $\text{C}_{\text{org}}/\text{P}$ ratio of the upper member of the Dengying Formation is less than 50, falling within the aerobic range, and the Ni/Co ratio is less than 7, corresponding to the dysoxic to aerobic range. In contrast, the $\text{C}_{\text{org}}/\text{P}$ ratio of the lower member of the Wangyinpu Formation exceeds 100, and its Ni/Co ratio is greater than 7, both of which fall within the anoxic range (Fig. 3e). The Mo_{EF} values range from 0.47 to 43.5 (average of 8.12), and the U_{EF} values range from 0.33 to

51.6 (average of 11.0), collectively exhibiting a pronounced characteristic of Mo and U enrichment (Fig. 3f). In addition, both indices exhibit a good synergistic variation trend, gradually increasing from bottom to top, indicating that the lower member of the Wangyinpu Formation exhibits more pronounced Mo and U enrichment compared to the upper member of the Dengying Formation (Fig. 3f).

4.3.3. Rare earth elements

The total rare earth element (\sum REE) contents of the studied samples range from 17.7 ppm to 184 ppm (average of 70.1 ppm), which are generally lower than \sum REE_{PAAS} (184.8 ppm) (McLennan, 1989). In addition, the ratios of the light REE and heavy REE contents (\sum LREE/ \sum HREE) of the samples range from 1.52 to 16.3 (average of 4.84), which are smaller than the value of \sum LREE_{PAAS}/ \sum HREE_{PAAS} (9.49). The rare earth distribution pattern is left-sloping (Fig. 5). Both of these characteristics indicate that the samples are enriched in heavy REEs. In addition, most of the samples exhibit positive Eu anomaly values (0.87–7.72, average of 1.63) and negative Ce anomaly values (0.48–1.14, average of 0.68) (Table S1 and Fig. 5). The siliceous shales in the lower part of the Wangyinpu Formation exhibit a very strong positive Eu anomaly (1.64–7.72, average of 3.53), which gradually decreases upward (Fig. 3g). Therefore, the samples from the PKC section are characterized by low \sum REE contents, heavy REE enrichment, positive to weakly negative Eu anomalies, and negative Ce anomalies.

5. Discussion

5.1. Increased paleo-productivity due to climate warming

5.1.1. Paleo-productivity

The abundance of OM in black shale is primarily controlled by two factors: the supply of organic material and the subsequent preservation conditions (Demaison and Moore, 1980; Leckie et al., 2002; Kuypers et al., 2002; Mort et al., 2007). The supply is closely linked to the paleo-productivity in the ancient ocean, with the elevated organic carbon flux in high productivity settings serving as a key prerequisite for OM enrichment of black shale (Kuypers et al., 2002; Leckie et al., 2002). Therefore, reconstructing the paleo-productivity is essential for understanding the mechanisms underlying OM accumulation in such deposits.

The TOC content is the most intuitive indicator of paleo-productivity. The TOC values of the samples from the lower member of the Wangyinpu Formation are significantly higher than those of the samples from the upper member of the Dengying Formation (Fig. 3a),

implying that the paleo-productivity gradually increased during the E–C transition. In addition, modern marine studies indicate that trace metals such as Zn and Ni often exhibit strong associations with OM due to their bioavailability and scavenging behavior (Bruland, 1989; Kuss and Kremling, 1999; Ribouleau et al., 2003; Pohl et al., 2004). As a result, Zn and Ni are frequently used as proxies for reconstructing paleo-productivity. In this study, we found that the Zn/Al and Ni/Al ratios of the Dengying Formation are significantly lower than those of the Wangyinpu Formation (Fig. 3d), suggesting a marked change in marine productivity during the E–C transition, which is consistent with the results indicated by the TOC data. Taken together, these results indicate that the marine productivity increased substantially from the Late Ediacaran to the Early Cambrian, likely reflecting broader climatic and environmental changes that occurred during this critical evolutionary interval. However, the weak correlations between the TOC and paleo-productivity proxies (e.g., Zn/Al and Ni/Al) (Fig. 6) indicate that marine productivity alone was not the sole factor controlling the OM enrichment of these black shales.

5.1.2. Climate warming

The CIA and ACNK ternary diagrams (with apices Al₂O₃, CaO + Na₂O, and K₂O) are widely used to assess the intensity of the chemical weathering of soils and sediments. They can also provide insights into regional and even global paleoclimate patterns (Algeo et al., 2025). However, several factors may influence CIA values, including grain size (Shao and Yang, 2012; Von Eynatten et al., 2012; Guo et al., 2018), provenance (Garzanti and Resentini, 2016; Algeo et al., 2025), sedimentary recycling (Gaillardet et al., 1999; Borges et al., 2008), and potassium metasomatism (Fedo et al., 1995; Panahi et al., 2000).

In this study, the factors that could potentially interfere with the CIA values were evaluated as follows: (a) All of the samples are fine-grained siliciclastic rocks with a high degree of homogeneity, which minimizes the influence of the grain size on the CIA values. (b) TiO₂ vs. Zr plots (Fig. 7a) indicate that the source rocks are intermediate to felsic igneous rocks. Th/Sc vs. Zr/Sc plots (Fig. 7b) further confirm that the lithology of the provenance was predominantly felsic, which is consistent with the above inference. (c) The low Zr/Sc ratios (Fig. 7b) suggest minimal sedimentary recycling and strong control by source rocks, supporting the use of CIA as a proxy for the weathering intensity in the source area. (d) On the ACNK diagrams, the sample compositions are nearly parallel to the A–K trend, and most of the samples plot below the illite pole (Fig. 7c). This indicates extensive loss of CaO and Na₂O relative to K₂O, which is consistent with the preferential breakdown of plagioclase over

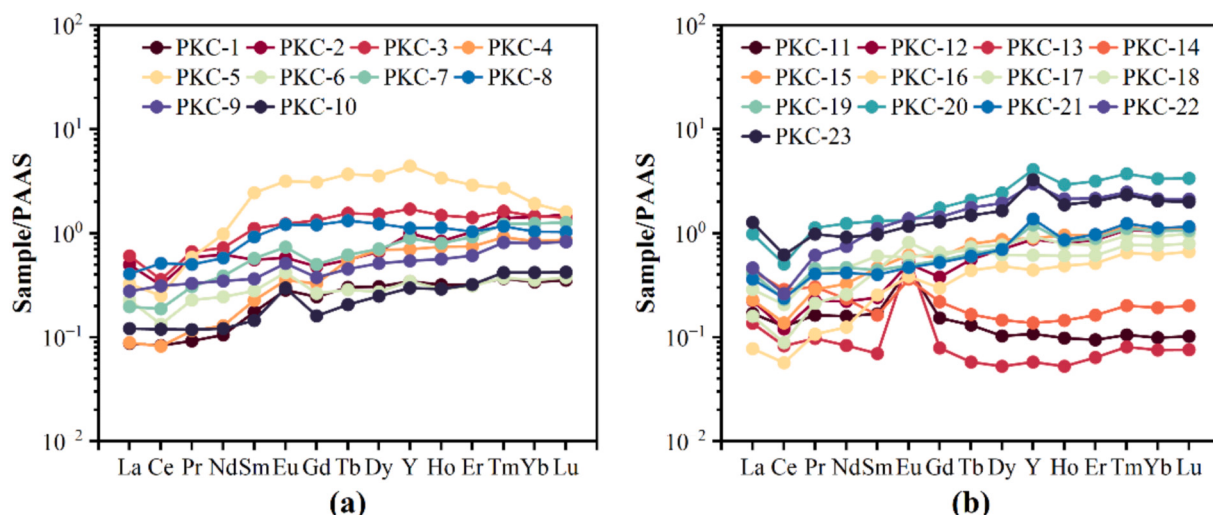


Fig. 5. (a) PAAS-normalized rare earth element compositions of the upper member samples of the Dengying Formation; (b) The lower member sample of the Wangyinpu Formation.

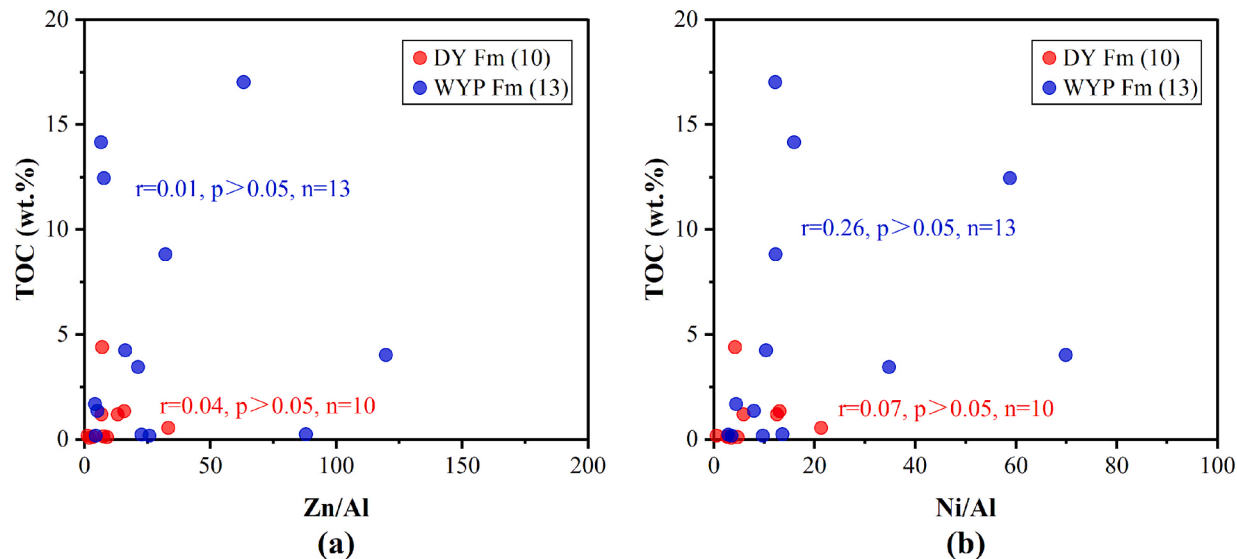


Fig. 6. Cross plot of TOC and Zn/Al for the samples in this study; (b) TOC vs. Ni/Al.

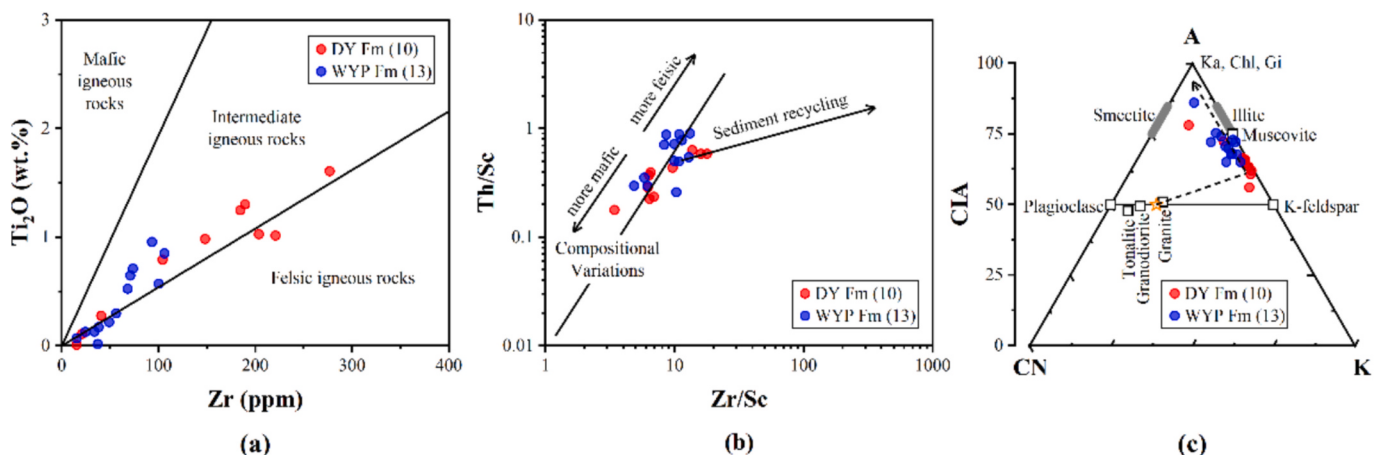


Fig. 7. (a) Ti₂O versus Zr diagram showing mineral composition variations (after Hayashi et al., 1997); (b) Th/Sc-Zr/Sc bivariate diagram showing mineral composition variations and sediment recycling (after McLennan et al., 1993); (c) A-CN-K ternary diagram of the samples from the PKC Section, Tonalite, granodiorite, and granite data are from (Taylor and McLennan, 1985), A-Al₂O₃, CN-CaO* + Na₂O, K-K₂O (all in molar proportions). Ka-kaolinite; Chl-chlorite; Gi-gibbsite; DY Fm = Dengying Formation, WYP Fm. = Wangyinpu Formation. The same conventions apply hereinafter.

potassium feldspar. This observation is further supported by the presence of potassium feldspar in the SEM images (Fig. 4).

Therefore, the inferred weathering path likely extends from intermediate-felsic igneous sources to a point below the illite pole and then toward the A apex (Fig. 7c). This pattern is typical of granitic to tonalitic source rocks (White et al., 2001; Liu et al., 2016; Algeo et al., 2025). No excess K is observed, indicating that potassium metasomatism did not affect the samples. Thus, the CIA values calculated in this study can reliably reflect the paleoclimate conditions of the source region.

For the samples deposited during the E-C transition, the CIA values ranged from 56.2 to 86.2, with an average of 68.9, indicating a generally warm and humid climate and moderate to strong weathering conditions. The CIA values in the Early Cambrian samples (65.2–86.2, average of 71.4) are higher than those of the Late Ediacaran samples (56.2–78.3, average of 64.2), exhibiting an overall increasing trend across the E-C transition (Fig. 3c and Fig. 7c). This suggests gradual warming of the climate and the intensification of chemical weathering during this transitional period. CIA data from previous studies also indicate that during the E-C transition, the climate in the Yangtze region tended to gradually warm, and this was accompanied by enhanced chemical

weathering (Zhai et al., 2018; Li et al., 2020; Zhang et al., 2021; Zhang et al., 2022a, 2022b). This is consistent with the findings of this study.

The climate warming and enhanced chemical weathering during this period suggest that intensification of terrestrial weathering and erosion occurred. The K/Al ratio is an effective indicator for reconstructing continental weathering, with lower K/Al values in marine sediments indicating a higher contribution from continental weathering (Ouyang et al., 2025). The samples from the lower Wangyinpu Formation and the upper Dengying Formation have K/Al values ranging from 0.12 to 1.01 (average of 0.60), which are generally higher than K/Al_{PAAAS} (0.31) (Fig. 3c), suggesting that the contribution of continental weathering to the marine sediments in the study area was limited during this period. This is consistent with the tectonic setting of the region during this period (Fig. 1b). Specifically, the K/Al values of the samples from the lower Wangyinpu Formation (0.18–1.01, average of 0.77) are significantly lower than those of the samples from the upper Dengying Formation (0.12–0.71, average of 0.51), indicating that the contribution from continental weathering increased during the E-C transition.

Terrestrial detritus is a crucial source of nutrients in seawater, and the gradual increase in the proportion of continental weathering

suggests an increase in the nutrient input from terrestrial sources. Nutrient supply and cycling are key factors controlling marine productivity. The Yangtze Block experienced widespread upwelling during the E–C transition (Pi et al., 2013; Liu et al., 2018; Wu et al., 2020a, 2020b; Fan et al., 2021; Li et al., 2022a, 2022b; Cañadas et al., 2024). This is critical for exchange between mid-depth and surface waters, which allows nutrients to be recycled within the upper water column, sustaining marine primary productivity. During the deposition of the upper Dengying Formation, the relatively cooler climate and weaker chemical weathering resulted in the limited transport of nutrients by rivers and wind into marginal seas, and thus, the marine productivity was restricted as a result of the limited availability of bioavailable nutrients in the seawater.

However, during the E–C transition, under the conditions of climate warming and increased chemical weathering, the flux of terrestrial nutrients increased, and these nutrients entered the biogeochemical cycle via the upwelling process, leading to a significant increase in productivity. Additionally, climate warming may have intensified monsoons, further enhancing the upwelling intensity and accelerating nutrient cycling, thereby promoting a dramatic surge in productivity. Consequently, during the E–C transition, climate warming indirectly contributed to the increase in the marine productivity in the Yangtze region. The increased organic carbon flux provided the necessary material basis for the formation of OM-rich black shale.

5.2. Expansion of dynamic hypoxia caused by water cycle obstruction

The preservation of OM is closely related to the redox conditions of the water column, which constitute another key factor controlling OM enrichment (Demaison and Moore, 1980; Mort et al., 2007). Anoxic or sulfidic bottom water reduces the rate of OM mineralization and promotes the burial of organic carbon. Therefore, reconstructing paleoredox conditions is essential for understanding the mechanisms of OM accumulation in black shale.

Several geochemical proxies are widely used for this purpose, including C_{org}/P (Algeo and Ingall, 2007), Ni/Co (Jones and Manning, 1994), and Mo_{EF} – U_{EF} covariation patterns (Algeo and Tribouillard, 2009; Tribouillard et al., 2012). Although these proxies may not reflect the absolute redox states, they effectively characterize the relative trends of the oxygenation level (Liu et al., 2017).

In this study, we found that the C_{org}/P and Ni/Co ratios of the Dengying Formation are both significantly lower than those in the Wangyinpu Formation (Fig. 3e). Moreover, on the Mo_{EF} – U_{EF} plot (Fig. 8a), the samples from the Wangyinpu Formation predominantly plot within the anoxic field, while those from the Dengying Formation exhibit more oxic to suboxic signatures. These observations indicate that

the extent of the anoxia expanded during the E–C transition, and intensified bottom-water anoxia occurred in the Early Cambrian.

Additionally, the Mo_{EF} – U_{EF} plot reveals that the uranium enrichment was greater than the molybdenum enrichment, suggesting the occurrence of strong hydrographic restriction. This is further supported by the Mo–TOC plot (Fig. 8b), in which most of the samples plot within the strongly restricted field. These features can be attributed to the geographic setting: the study area was situated between the Yangtze carbonate platform and the Jiangnan paleo-uplift. The presence of the paleo-uplift limited the exchange of water between the basin and the open ocean, leading to the development of a semi-restricted basin. Under such conditions, deep-water renewal was limited, favoring the establishment of anoxic bottom water. Under the climate warming during the E–C transition (see Section 5.1), the oceanic circulation slowed as a result of the greenhouse conditions, the stratification of the water column intensified, and the vertical mixing weakened—all of which further enhanced the water-column anoxia.

In addition, under anoxic and reducing conditions, SRB can utilize various forms of OM as carbon sources and can utilize SO_4^{2-} as electron acceptors to drive OM oxidation. BSR is responsible for more than 50 % of the TOC oxidation in marine sediments (Canfield et al., 1993; Jørgensen, 1982). Therefore, the intensity of BSR should also be considered when evaluating OM enrichment. Lallier-Vergès et al. (1993) proposed the SRI as a proxy for the BSR intensity, with higher SRI values indicating stronger BSR activity. The TOC vs. SRI plot (Fig. 8c) shows that the samples from the Wangyinpu Formation have lower SRI values compared to those of the samples from the Dengying Formation, suggesting that the BSR intensity decreased during the E–C transition. This weakening of the BSR process reduces the consumption of OM, thereby allowing more organic carbon to be buried.

Furthermore, the TOC exhibits significant positive correlations with the redox proxies C_{org}/P and Ni/Co (Fig. 9), further supporting the interpretation that changes in the redox conditions were the primary factors controlling the formation of marine OM-rich shales during the E–C transition. The development of OM-rich black shales was driven by environmental conditions such as restricted water circulation and enhanced water column stratification, which were induced by the semi-enclosed basin setting and greenhouse climate. These conditions promoted the expansion of the anoxic bottom water, providing favorable preservation conditions for OM accumulation. Additionally, the inhibition of BSR likely reduced the oxidation of organic carbon to some extent, further facilitating the burial of organic carbon.

5.3. Dilution of OM via hydrothermal Si enrichment

Identification of hydrothermal sediment signatures is a critical step

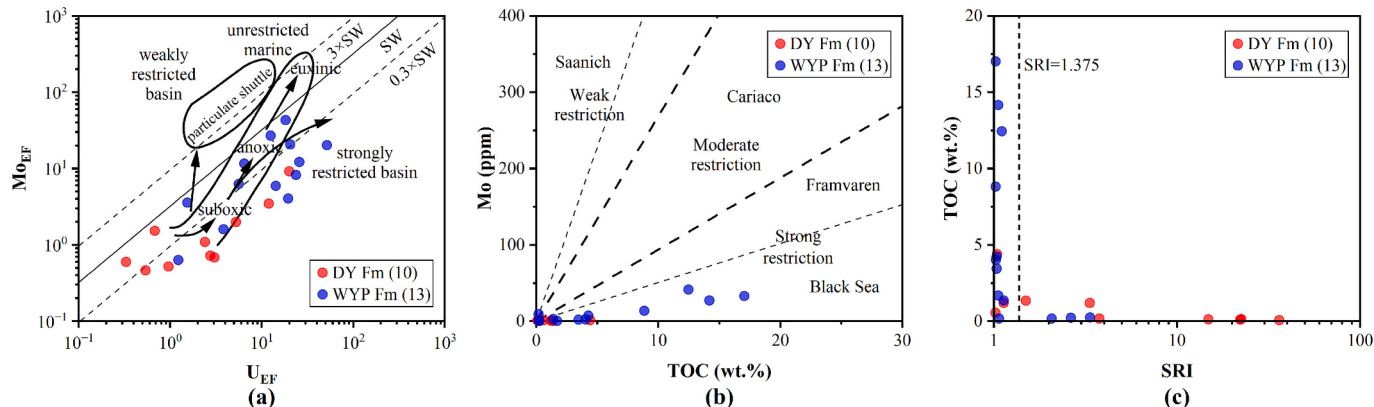


Fig. 8. (a) Shows a crossplot of Mo_{EF} versus U_{EF} for the samples in this study, adapted from Algeo and Tribouillard (2009) and Tribouillard et al. (2012); (b) illustrates the relationship between Mo and TOC, adapted from Algeo and Lyons (2006) and Algeo et al. (2007); (c) Shows a cross plot of TOC and SRI for the samples in this study, adapted from Liu et al. (2021).

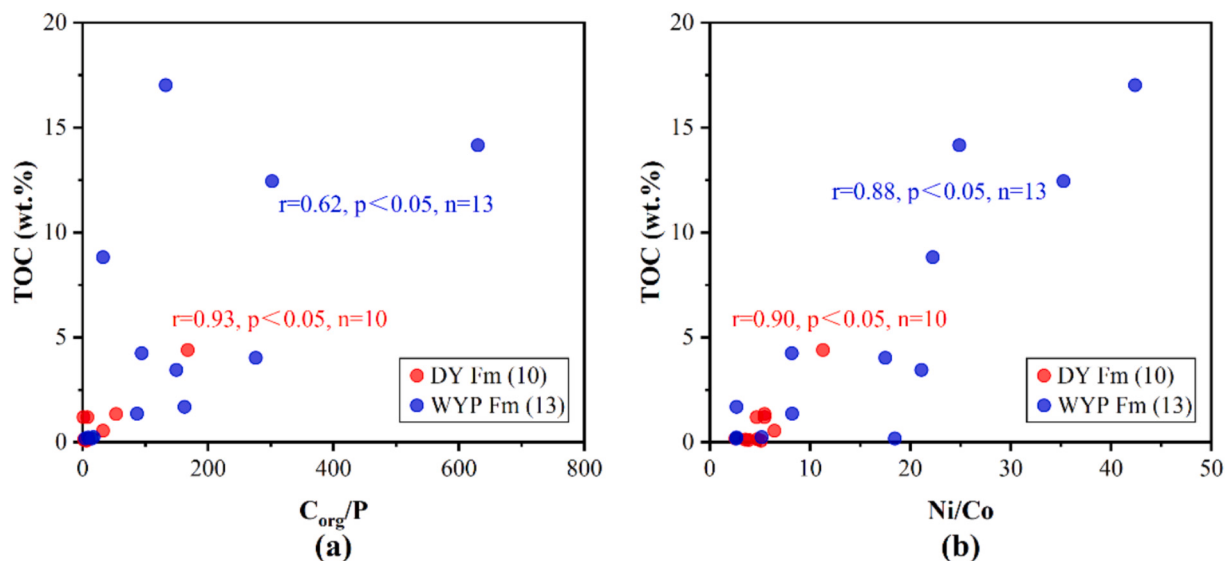


Fig. 9. Cross plot of TOC and C_{org}/P for the samples in this study; (b) TOC vs. Ni/Co.

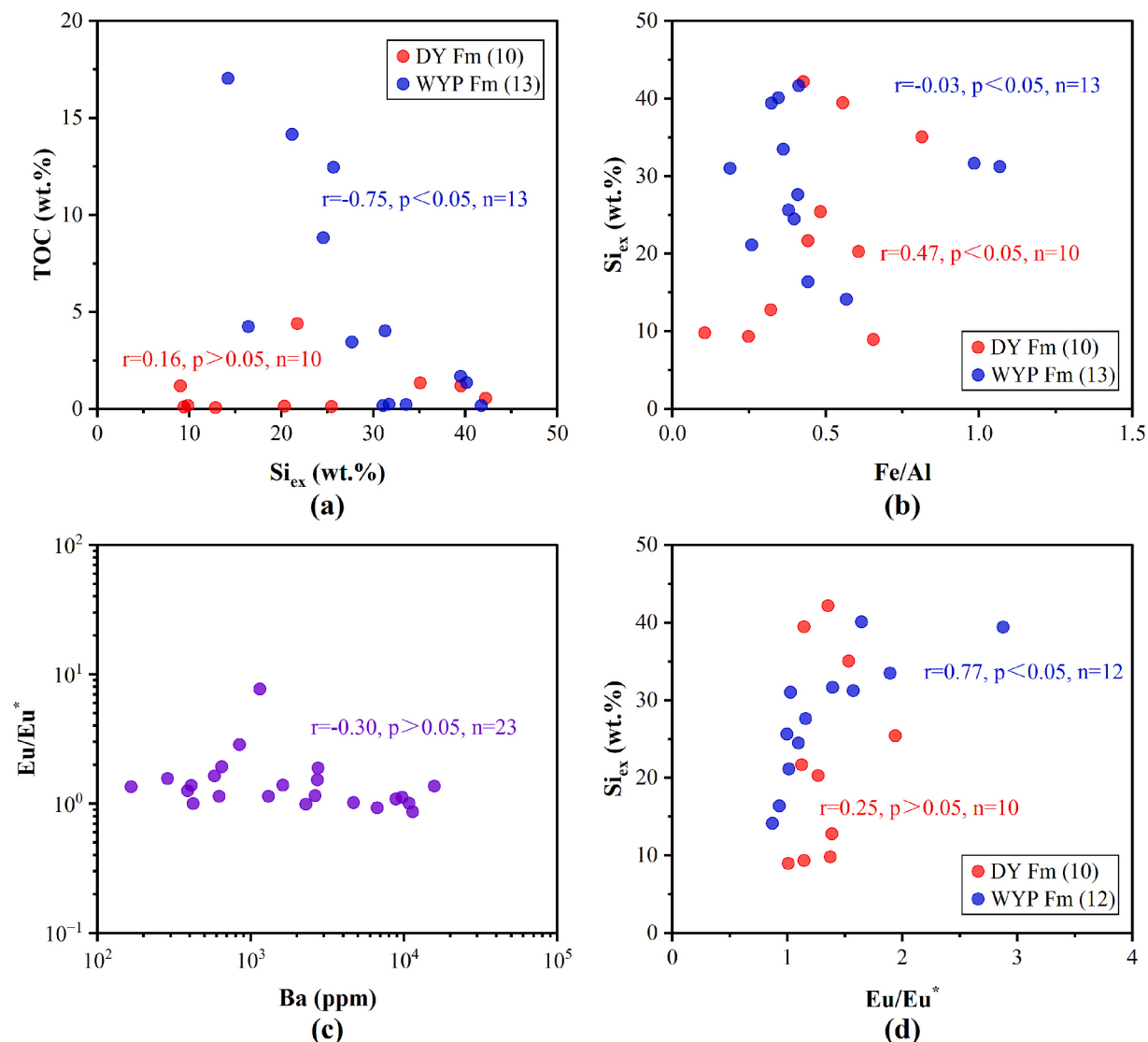


Fig. 10. (a) Cross plot of TOC and Si_{ex} for the samples in this study; (b) TOC vs. Fe/Al; (c) Eu/Eu^* vs. Ba, and (d) Si_{ex} vs. Eu/Eu^* .

in reconstructing the marine paleoenvironment. Hydrothermal metal-rich sediments are typically characterized by low $\sum\text{REE}$ concentrations, enrichment of LREEs, positive to weakly negative Eu anomalies, and negative Ce anomalies (Marchig et al., 1982; Fleet, 1983). The REE geochemical signatures of the samples analyzed in this study clearly exhibit such hydrothermal sedimentary features (Fig. 3g).

The mineralogical evidence further supports this interpretation: zoned hyalophane, which is commonly associated with Ba-rich hydrothermal fluids and is considered to be a typical hydrothermal mineral (Han et al., 2015; Wu et al., 2020a, 2020b), is present in all of the samples (Fig. 4). Therefore, continuous hydrothermal fluid activity occurred in the study area during the E–C transition.

Moreover, hyalophane has been widely reported to occur in Lower Cambrian black shales across the Yangtze Platform (Wu, 2000; Han et al., 2015; Chang et al., 2018; Huang et al., 2018; Wu et al., 2020a, 2020b; Liu et al., 2023; Dong et al., 2025), and its spatial distribution closely corresponds to that of the Jiangnan deep fault Zone—a major Caledonian fault zone along the southeastern margin of the Yangtze Platform (Fig. 2). This spatial correlation suggests that the distribution of these hydrothermal deposits along the southeastern margin of the Yangtze Platform was structurally controlled by marginal deep faults during the E–C transition. This hydrothermal activity would have supplied large amounts of DSi, playing an important role in the development of C-rich, high-silica black shales during this transitional period.

However, a high content of siliceous fractions may exert a potential dilution effect on OM (Chu et al., 2016; Dong et al., 2025; Zhou et al., 2024). Therefore, a deeper understanding of the Si cycle is essential for elucidating the mechanisms of OM enrichment. In addition to terrigenous clastics derived from continental weathering, the siliceous fractions in black shale primarily originate from biogenic processes and hydrothermal inputs (Zhang et al., 2018; Dong et al., 2019; Xi et al., 2019).

Given that the study area was a hydrothermal sedimentary setting, no obvious positive correlation between TOC and Si_{ex} was observed (Fig. 10a). Furthermore, the SEM observations reveal the presence of abundant cryptocrystalline silica and few biogenic remains (Fig. 3), indicating that biogenic silica was not the dominant source of the Si_{ex} and that hydrothermal input was the primary contributor. Previous studies have documented the occurrence of coupling between the Si and Fe cycles in chert (Li et al., 2022a, 2022b; Tostevin and Sevgen, 2024). We suggest that a similar coupling may also be present in C-rich, high-silica black shales.

Tostevin and Sevgen (2024) proposed an Fe(II)–silicate gel adsorption and Si dissolution model to explain the transport and burial of silica in marine settings. During the E–C transition, continuous hydrothermal activity could have supplied sufficient Fe^{2+} and H_2SiO_3 to form Fe(II)–silicate gels. The formation and preservation of these gels in seawater are closely tied to the redox conditions. The expansion of anoxic water masses during the E–C transition would have favored the stabilization and preservation of Fe(II)–silicate gels, facilitating the transport of hydrothermal-derived silica over broader regions centered on hydrothermal vents.

In addition, Eu/Eu^* is commonly associated with hydrothermal activity (Steiner et al., 2001; Chen et al., 2009; Li et al., 2015; Migdisov et al., 2016). However, Ba may interfere with Eu/Eu^* during analysis, potentially causing false anomalies (Wu et al., 2020). In this study, we found that Ba does not exhibit an obvious correlation with Eu/Eu^* (Fig. 10c); therefore, the calculated Eu/Eu^* values are reliable. Therefore, in this study, we used the Eu/Eu^* to represent the hydrothermal intensity and the Fe/Al ratio to represent the flux of Fe(II)–silicate gels. For the samples from the upper member of the Late Ediacaran Dengying Formation, Si_{ex} exhibits a certain positive correlation with Fe/Al but only a weak correlation with Eu/Eu^* (Figs. 10b and c), indicating that under oxic or low-oxygen conditions, the flux of Fe(II)–silicate gels was the primary factor controlling the burial of NTS. In addition, high $\text{Si}_{\text{ex}}/\text{Fe}$ ratios indicate substantial Fe loss during burial, possibly due to

remobilization into seawater caused by benthic bioturbation or similar processes. Furthermore, for the samples from the lower member of the Lower Cambrian Wangyinpu Formation, Si_{ex} exhibits a weak correlation with Fe/Al (Fig. 10b), which may be attributed to the co-adsorption of dissolved OM and DSi onto Fe(II)–silicate gels under high productivity conditions (see Section 5.1), thus leading to unstable Fe/Si burial ratios. OM mineralization may also cause disaggregation of such gels, thereby reducing the burial of hydrothermal Si. In addition, for the samples from the lower member of the Wangyinpu Formation, Si_{ex} exhibits a certain positive correlation with Eu/Eu^* (Fig. 10c), indicating that under expanded dynamic anoxia, the hydrothermal intensity became the main factor controlling the NTS flux. Increased hydrothermal activity enhances the input of hydrothermal Si, resulting in a pronounced dilution effect on OM. This is confirmed by the significant negative correlation between the TOC and Si_{ex} contents of the samples from the Wangyinpu Formation (Fig. 10a).

5.4. NTS–OM co-evolution model under the control of dynamic hypoxia

During the E–C transition, continuous hydrothermal activity along the southeastern margin of the Yangtze Platform played a crucial role in the formation of black shales in deep-water and semi-deep water settings (Li et al., 2015; Wu et al., 2020; Zhang et al., 2020; Zhou et al., 2024; Dong et al., 2025). Si-rich fluids emanating from the Jiangnan deep fault significantly modified the conditions of the marine environment at that time, influencing both the deposition of NTS and the accumulation of OM in these black shales.

We propose that the co-evolution of NTS and OM was not solely controlled by hydrothermal activity but was also strongly influenced by the expansion of the dynamic anoxic zone and organic carbon burial flux. To better elucidate these processes, we present a new conceptual model to clarify the formation mechanism of the C-rich, high-silica black shales in the deep-bathyal environment of the southeastern Yangtze Platform during the E–C transition and to reveal the co-evolutionary dynamics of the NTS and OM in such a setting (Fig. 11). A detailed analysis is provided below.

During the E–C transition, regional and possibly global climate warming triggered an increase in paleo-oceanic productivity in the deep-water and semi-deep water settings of the Yangtze Platform, South China. Concurrently, restricted water circulation led to significant expansion of the dynamic anoxic zone (Figs. 11a and b). These changes in the marine environment created favorable conditions for OM accumulation, with the enhanced productivity ensuring a high OM supply and the expanded anoxia promoting its preservation. Together, these factors provided the essential prerequisites for the formation of OM-rich black shales during the E–C transition. In addition, submarine hydrothermal activity associated with the Jiangnan deep fault zone released substantial amounts of Fe^{2+} and H_4SiO_4 into the seawater (Fig. 11c). Near the associated hydrothermal vents, hydrothermal-derived silica could precipitate directly from saturated Si-rich fluids (Siever, 1992). However, in the broader regions surrounding the vents, silica was transported in the form of Fe(II)–silicate gels (Figs. 11d and e) (Tostevin and Sevgen, 2024). This process facilitated the widespread input of hydrothermal silica into the marine sediments, which may have exerted a dilution effect on the OM accumulation (Chu et al., 2016; Zhou et al., 2024; Dong et al., 2025).

The formation, migration, and burial of these Fe(II)–silicate gels were primarily controlled by the extent of the bottom-water anoxia and the flux of the organic carbon deposition. Near the chemocline, hydrothermally derived Fe^{2+} and H_2SiO_3 undergo coordination, hydrolysis, and polymerization to form abundant nanoscale Fe(II)–silicate gels (Fig. 11c) (Halevy et al., 2017; Rasmussen et al., 2017; Hinz et al., 2021). Owing to their large specific surface area, these gels can absorb significant amounts of DSi and organic particles. When the dynamic anoxic zone expands and the chemocline rises, Fe(II)–silicate gels remain suspended in the water column for extended periods of time due

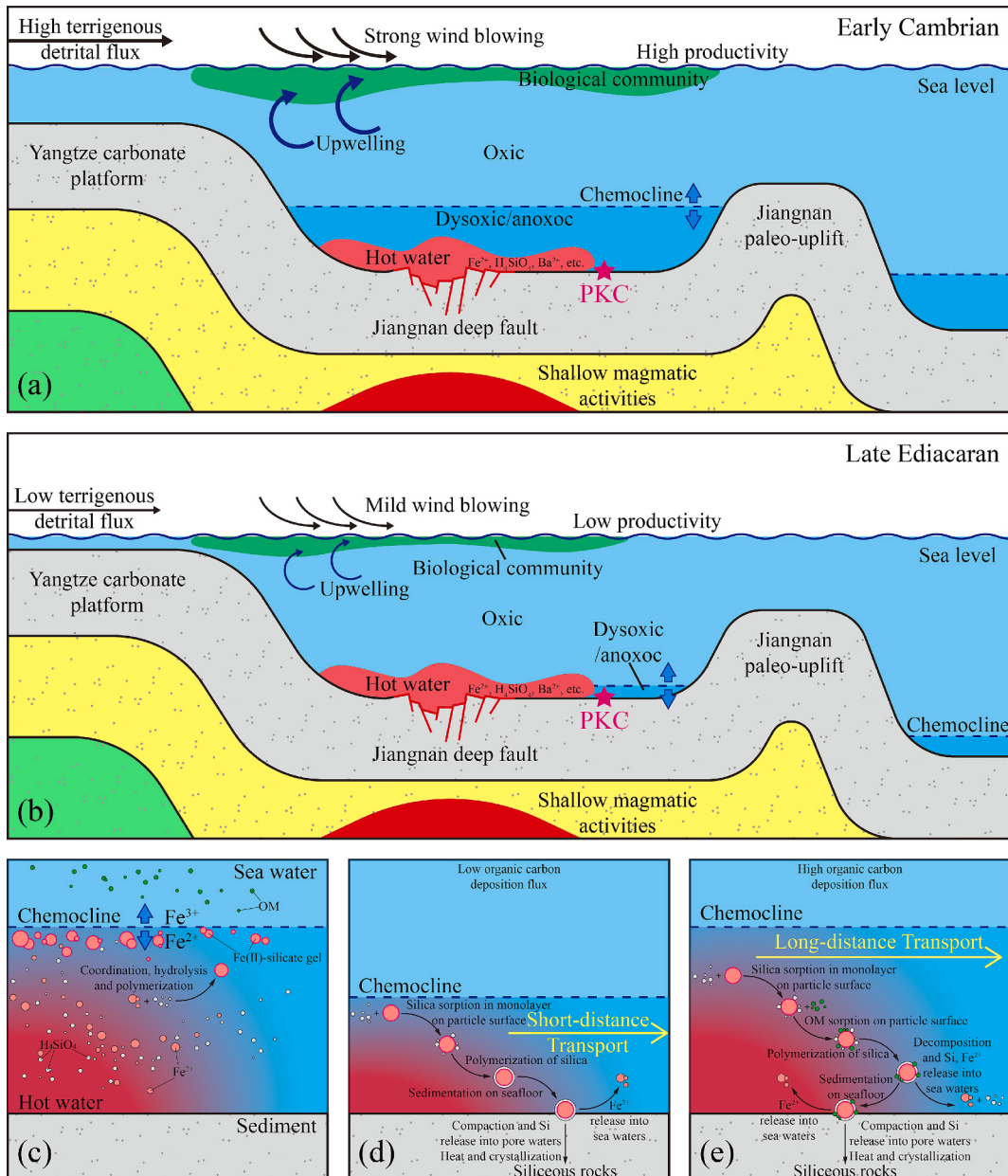


Fig. 11. Conceptual model for the co-evolution of NTS and OM during the E-C transition. (a) (b) Paleoenvironmental evolution of the deep- to semi-deep water settings along the southeastern margin of the Yangtze Platform during the E-C transition; (c) Source of hydrothermal-derived silica and formation of Fe (II)-silicate gels; (d) (e) Schematic diagram of NTS deposition. During settling, Fe(II)-silicate gels adsorb both hydrothermal-derived silica and OM particles. With the expansion of the dynamic anoxic zone, the residence time of the gels in the water column increases, allowing for longer lateral transport distances. Differences in primary productivity led to variations in the types and amounts of particles adsorbed by the gels.

to the slow settling rate of nanoparticles (Tostevin and Sevgen, 2024), thereby increasing their lateral transport distance (Figs. 11d and e). This implies that under expanded anoxic conditions, more hydrothermal-derived Si can be transported away from vent sites in the form of Fe (II)-silicate gels. As the hydrothermal activity intensifies, the flux of hydrothermal Si to the surrounding sediments increases, potentially exerting a dilution effect on OM accumulation. Conversely, when the oxygen levels in the water column are relatively high, the transport capacity of Fe(II)-silicate gels is limited, which constrains the deposition flux of non-terrigenous silica derived from hydrothermal sources.

In addition, under high primary productivity conditions, the supply of OM increases. Fe(II)-silicate gels adsorb both DSi and OM particles; however, OM may compete for adsorption sites, thereby reducing the amount of DSi carried by the gels. When these OM-adsorbed gels settle

to the seafloor, partial disintegration can occur due to mineralization of the OM, leading to the release of Si and Fe into the pore water (Fig. 11e). Thus, an increase in the OM flux may inhibit the burial of hydrothermal-derived Si to some extent, resulting in reduced Si deposition and a weakened dilution effect on OM. Moreover, during early diagenesis, physical processes such as compaction can cause the breakdown of Fe (II)-silicate gels. Upon disintegration, Si and Fe are released into the formation water (Rasmussen and Muhling, 2021). Due to its relatively low solubility, Si tends to precipitate as cryptocrystalline silica, whereas Fe remains more soluble and can be expelled into the overlying seawater via compaction-driven fluid flow, leading to significant Fe loss (Figs. 11d and e). This preferential retention of Si over Fe likely explains the generally high S_{ex}/Fe ratios of the rocks analyzed in this study.

6. Conclusions

1. During the E-C transition, climate warming significantly enhanced marine productivity in the deep- to semi-deep water zones of the southeastern Yangtze Platform, while the restricted water circulation triggered the expansion of dynamic anoxic zones. These two factors respectively provided supply and preservation conditions for the formation of OM-rich black shales.

2. Hydrothermal fluids from deep faults in the margin of the platform delivered abundant hydrothermal Si to the region, which diffused in the form of Fe(II)-silicate gels. The extent of the marine dynamic anoxia regulated the sedimentation flux of NTS to distal areas around the vents by influencing the migration distance of the Fe(II)-silicate gels: under oxic conditions, the short migration distances limited the NTS flux; under anoxic conditions, the longer migration distances increased the NTS flux as a result of enhanced hydrothermal activity, promoting NTS enrichment of the sediments.

3. Anoxia facilitated both OM accumulation and NTS enrichment (which diluted the OM), maintaining a dynamic balance between the OM and NTS. Thus, the water oxygenation level served as the key factor controlling the OM-NTS co-evolution in this region during the E-C transition. This verifies that changes in the redox state were a core driving force during the early evolution of the Earth.

CRediT authorship contribution statement

Hezheng Dong: Writing – original draft, Visualization, Software, Investigation, Formal analysis, Data curation. **Dongsheng Zhou:** Writing – review & editing, Writing – original draft, Supervision, Resources, Project administration, Methodology, Investigation, Conceptualization. **Yufei Liang:** Software, Investigation. **Lei Huang:** Software, Investigation, Data curation.

Declaration of competing interest

The authors declare that they have no known competing financial interests or personal relationships that could have appeared to influence the work reported in this paper.

Data availability

The authors confirm that all data necessary for supporting the scientific findings of this paper have been provided.

Acknowledgement

This study was funded by the Ministry of Natural Resources, Peoples Republic of China (project: evaluation of shale gas resources and selection of favorable areas in the Middle and Lower Yangtze areas). We are deeply indebted to the editor and the two anonymous reviewers for their invaluable and constructive suggestions, which have significantly enhanced the quality of this manuscript.

Appendix A. Supplementary data

Supplementary data to this article can be found online at <https://doi.org/10.1016/j.palaeo.2025.113301>.

References

- Algeo, T.J., Ingall, E., 2007. Sedimentary Corg:P ratios, paleocean ventilation, and Phanerozoic atmospheric pO₂. *Palaeogeogr. Palaeoclimatol. Palaeoecol.* 256, 130–155. <https://doi.org/10.1016/j.palaeo.2007.02.029>.
- Algeo, T.J., Lyons, T.W., 2006. Mo-total organic carbon covariation in modern anoxic marine environments: Implications for analysis of paleoredox and paleohydrographic conditions: MO-TOC COVARIATION IN ANOXIC SEDIMENTS. *Paleoceanography* 21, n/a-n/a. <https://doi.org/10.1029/2004PA001112>.
- Algeo, T.J., Tribouillard, N., 2009. Environmental analysis of paleoceanographic systems based on molybdenum–uranium covariation. *Chem. Geol.* 268, 211–225. <https://doi.org/10.1016/j.chemgeo.2009.09.001>.
- Algeo, T.J., Hannigan, R., Rowe, H., Brookfield, M., Baud, A., Krystyn, L., Ellwood, B.B., 2007. Sequencing events across the Permian–Triassic boundary, Guryul Ravine (Kashmir, India). *Palaeogeogr. Palaeoclimatol. Palaeoecol.* 252, 328–346. <https://doi.org/10.1016/j.palaeo.2006.11.050>.
- Algeo, T.J., Hong, H., Wang, C., 2025. The chemical index of alteration (CIA) and interpretation of ACNK diagrams. *Chem. Geol.* 671, 122474. <https://doi.org/10.1016/j.chemgeo.2024.122474>.
- Amthor, J.E., Grotzinger, J.P., Schröder, S., Bowring, S.A., Ramezani, J., Martin, M.W., Matter, A., 2003. Extinction of Cloudina and Namacalathus at the Precambrian–Cambrian boundary in Oman. *Geology* 31, 431. [https://doi.org/10.1130/0091-7613\(2003\)031<0431:ecana>2.0.co;2](https://doi.org/10.1130/0091-7613(2003)031<0431:ecana>2.0.co;2).
- Beauchamp, B., Baud, A., 2002. Growth and demise of Permian biogenic chert along northwest Pangea: evidence for end-Permian collapse of thermohaline circulation. *Palaeogeogr. Palaeoclimatol. Palaeoecol.* 184, 37–63. [https://doi.org/10.1016/s0031-0182\(02\)00245-6](https://doi.org/10.1016/s0031-0182(02)00245-6).
- Borges, J.B., Hu, Y., Moon, S., Noh, H., 2008. Provenance and weathering control on river bed sediments of the eastern Tibetan Plateau and the Russian Far East. *Chem. Geol.* 254, 52–72. <https://doi.org/10.1016/j.chemgeo.2008.06.002>.
- Bruland, K.W., 1989. Complexation of zinc by natural organic ligands in the central North Pacific. *Limnol. Oceanogr.* 34, 269–285. <https://doi.org/10.4319/lo.1989.34.2.0269>.
- Calvert, S.E., Pedersen, T.F., 1993. Geochemistry of recent oxic and anoxic marine sediments: Implications for the geological record. *Mar. Geol.* 113, 67–88. [https://doi.org/10.1016/0025-3227\(93\)90150-t](https://doi.org/10.1016/0025-3227(93)90150-t).
- Cañadas, F., Papineau, D., Algeo, T.J., Li, C., 2024. Upwelling-driven high organic production in the late Ediacaran. *Commun Earth Environ* 5, 461. <https://doi.org/10.1038/s43247-024-01632-z>.
- Canfield, D.E., Jørgensen, B.B., Fossing, H., Glud, R., Gunderson, J., Ramsing, N.B., Thamdrup, B., Hansen, J.W., Nielsen, L.P., Hall, P.O.J., 1993. Pathways of organic carbon oxidation in three continental margin sediments. *Mar. Geol.* 113, 27–40. [https://doi.org/10.1016/0025-3227\(93\)90147-n](https://doi.org/10.1016/0025-3227(93)90147-n).
- Chang, C., Hu, W.-X., Fu, Q., Cao, J., Wang, X.-L., Wan, Y., Yao, S.-P., 2018. Characteristics and formation processes of (Ba, K, NH₄)-feldspar and cymrite from a lower Cambrian black shale sequence in Anhui Province, South China. *Mineral. Mag.* 82, 1–21. <https://doi.org/10.1180/minmag.2017.081.017>.
- Chang, L., Zhang, S., Li, H., Xian, H., Wu, H., Yang, T., 2022. New Paleomagnetic Insights into the Neoproterozoic connection between South China and India and their Position in Rodinia. *Geophys. Res. Lett.* 49. <https://doi.org/10.1029/2022GL098348>.
- Chen, D., Wang, J., Qing, H., Yan, D., Li, R., 2009. Hydrothermal venting activities in the early Cambrian, South China: Petrological, geochronological and stable isotopic constraints. *Chem. Geol.* 258, 168–181. <https://doi.org/10.1016/j.chemgeo.2008.10.016>.
- Chu, C.L., Chen, L.Q., Zhang, B., Jiang, H.J., Yang, X., 2016. Influence on Formation of Yuertusi Source Rock by Hydrothermal Activities at Dongergou Section Tarim Basin. *Acta Sedimentol. Sin.* 34, 803–810. <https://doi.org/10.14027/j.cnki.cjxb.2016.04.020> (in Chinese with English abstract).
- Conley, D.J., Frings, P.J., Fontorbe, G., Clymans, W., Stadmark, J., Hendry, K.R., Marron, A.O., De La Rocha, C.L., 2017. Biosilicification Drives a Decline of Dissolved Si in the Oceans through Geologic Time. *Front. Mar. Sci.* 4. <https://doi.org/10.3389/fmars.2017.00039>.
- Craig, J. (Ed.), 2009. *Global Neoproterozoic Petroleum Systems: The Emerging Potential in North Africa*, Geological Society Special Publications. Geological Society, London.
- Demaison, G.J., Moore, G.T., 1980. Anoxic environments and oil source bed genesis. *Org. Geochem.* 2, 9–31. [https://doi.org/10.1016/0146-6380\(80\)90017-0](https://doi.org/10.1016/0146-6380(80)90017-0).
- Dong, T., He, S., Chen, M., Hou, Y., Guo, X., Wei, C., Han, Y., Yang, R., 2019. Quartz types and origins in the paleozoic Wufeng-Longmaxi Formations, Eastern Sichuan Basin, China: Implications for porosity preservation in shale reservoirs. *Mar. Pet. Geol.* 106, 62–73. <https://doi.org/10.1016/j.marpetgeo.2019.05.002>.
- Dong, H., Zhou, D., Huang, X., Liang, Y., Huang, L., Xu, J., 2025. Do hydrothermal fluids cause a dilution effect on organic matter in the early cambrian marine Black Shales? *Mar. Pet. Geol.* 107361. <https://doi.org/10.1016/j.marpetgeo.2025.107361>.
- Fan, H., Fu, X., Ward, J.F., Yin, R., Wen, H., Feng, X., 2021. Mercury isotopes track the cause of carbon perturbations in the Ediacaran Ocean. *Geology* 49, 248–252. <https://doi.org/10.1130/G48266.1>.
- Fedo, C.M., Wayne Nesbitt, H., Young, G.M., 1995. Unraveling the effects of potassium metasomatism in sedimentary rocks and paleosols, with implications for paleoweathering conditions and provenance. *Geology* 23, 921. [https://doi.org/10.1130/0091-7613\(1995\)023<0921:UTEOPM>2.3.CO;2](https://doi.org/10.1130/0091-7613(1995)023<0921:UTEOPM>2.3.CO;2).
- Fleet, A.J., 1983. Hydrothermal and hydrogenous ferro-manganese deposits: do they form a continuum? The rare earth element evidence. In: Rona, P.A., Boström, K., Laubier, L., Smith, K.L. (Eds.), *Hydrothermal Processes at Seafloor Spreading Centers*. Springer US, Boston, MA, pp. 535–555. https://doi.org/10.1007/978-1-4899-0402-7_23.
- Gaillardet, J., Dupré, B., Allégre, C.J., 1999. Geochemistry of large river suspended sediments: silicate weathering or recycling tracer? *Geochim. Cosmochim. Acta* 63, 4037–4051. [https://doi.org/10.1016/S0016-7037\(99\)00307-5](https://doi.org/10.1016/S0016-7037(99)00307-5).
- Gao, P., Li, S., Lash, G.G., He, Z., Xiao, X., Zhang, D., Hao, Y., 2020a. Silicification and Si cycling in a silica-rich ocean during the Ediacaran–Cambrian transition. *Chem. Geol.* 552, 119787. <https://doi.org/10.1016/j.chemgeo.2020.119787>.
- Gao, P., Li, S., Lash, G.G., He, Z., Xiao, X., Zhang, D., Hao, Y., 2020b. Silicification and Si cycling in a silica-rich ocean during the Ediacaran–Cambrian transition. *Chem. Geol.* 552, 119787. <https://doi.org/10.1016/j.chemgeo.2020.119787>.

- Garzanti, E., Resentini, A., 2016. Provenance control on chemical indices of weathering (Taiwan river sands). *Sediment. Geol.* 336, 81–95. <https://doi.org/10.1016/j.sedgeo.2015.06.013>.
- Guo, Y., Yang, S., Su, N., Li, C., Yin, P., Wang, Z., 2018. Revisiting the effects of hydrodynamic sorting and sedimentary recycling on chemical weathering indices. *Geochim. Cosmochim. Acta* 227, 48–63. <https://doi.org/10.1016/j.gca.2018.02.015>.
- Guo, X., Wang, R., Shen, B., Wang, G., Wan, C., Wang, Q., 2025. Geological characteristics, resource potential, and development direction of shale gas in China. *Pet. Explor. Dev.* 52, 17–32. [https://doi.org/10.1016/S1876-3804\(25\)60002-4](https://doi.org/10.1016/S1876-3804(25)60002-4).
- Halevy, I., Alesker, M., Schuster, E.M., Popovitz-Biro, R., Feldman, Y., 2017. A key role for green rust in the Precambrian oceans and the genesis of iron formations. *Nat. Geosci.* 10, 135–139. <https://doi.org/10.1038/ngeo2878>.
- Han, S., Hu, K., Cao, J., Pan, J., Xia, F., Wu, W., 2015. Origin of early Cambrian black-shale-hosted barite deposits in South China: Mineralogical and geochemical studies. *J. Asian Earth Sci.* 106, 79–94. <https://doi.org/10.1016/j.jseas.2015.03.002>.
- Hayashi, K.-I., Fujisawa, H., Holland, H.D., Ohmoto, H., 1997. Geochemistry of ~1.9 Ga sedimentary rocks from northeastern Labrador Canada. *Geochim. Cosmochim. Acta* 61, 4115–4137. [https://doi.org/10.1016/S0016-7037\(97\)00214-7](https://doi.org/10.1016/S0016-7037(97)00214-7).
- Hinz, I.L., Nims, C., Theuer, S., Templeton, A.S., Johnson, J.E., 2021. Ferric iron triggers greenalite formation in simulated Archean seawater. *Geology* 49, 905–910. <https://doi.org/10.1130/G48495.1>.
- Holdaway, H.K., Clayton, C.J., 1982. Preservation of shell microstructure in silicified brachiopods from the Upper cretaceous Wilmington Sands of Devon. *Geol. Mag.* 119, 371–382. <https://doi.org/10.1017/S0016756800026285>.
- Huang, Jianxun, Jin, J., Zhang, G., 1990. Regional Geology of Hubei Province. *Geology Press, Beijing*.
- Huang, K., Shao, Y., Sun, Y., Zhu, F., 2018. The metallogenetic regularity of Baoxi large barite deposit in Hunan Province. *West-China Explorat. Eng.* 30, 123–126 (in Chinese with English abstract).
- Isley, A.E., 1995. Hydrothermal Plumes and the delivery of Iron to Banded Iron Formation. *J. Geol.* 103, 169–185. <https://doi.org/10.1086/629734>.
- Jiang, G., Shi, X., Zhang, S., Wang, Y., Xiao, S., 2011. Stratigraphy and paleogeography of the Ediacaran Doushantuo Formation (ca. 635–551Ma) in South China. *Gondwana Res.* 19, 831–849. <https://doi.org/10.1016/j.gr.2011.01.006>.
- Jones, B., Manning, D.A.C., 1994. Comparison of geochemical indices used for the interpretation of palaeoredox conditions in ancient mudstones. *Chem. Geol.* 111, 111–129. [https://doi.org/10.1016/0009-2541\(94\)90085-X](https://doi.org/10.1016/0009-2541(94)90085-X).
- Jørgensen, B.B., 1982. Mineralization of organic matter in the sea bed—the role of sulphate reduction. *Nature* 296, 643–645. <https://doi.org/10.1038/296643a0>.
- Jurkowska, A., Świerczewska-Gladysz, E., 2020. Evolution of late cretaceous Si cycling reflected in the formation of siliceous nodules (flints and cherts). *Glob. Planet. Chang.* 195, 103334. <https://doi.org/10.1016/j.gloplacha.2020.103334>.
- Kuss, J., Kremling, K., 1999. Particulate trace element fluxes in the deep Northeast Atlantic Deep Sea. *Deep Sea Res. Part Oceanogr. Res. Pap.* 46, 149–169. [https://doi.org/10.1016/S0967-0637\(98\)00059-4](https://doi.org/10.1016/S0967-0637(98)00059-4).
- Kuypers, M.M.M., Pancost, R.D., Nijenhuis, I.A., Sinninge Damsté, J.S., 2002. Enhanced productivity led to increased organic carbon burial in the euxinic North Atlantic basin during the late Cenomanian oceanic anoxic event: enhanced productivity during C/T OAE-2. *Paleoceanography* 17. <https://doi.org/10.1029/2000PA000569>, 3–13–13.
- Lallier-Vergès, E., Bertrand, P., Desprairies, A., 1993. Organic matter composition and sulfate reduction intensity in Oman margin sediments. *Mar. Geol.* 112, 57–69. [https://doi.org/10.1016/0025-3227\(93\)90161-N](https://doi.org/10.1016/0025-3227(93)90161-N).
- Leckie, R.M., Bralower, T.J., Cashman, R., 2002. Oceanic anoxic events and plankton evolution: Biotic response to tectonic forcing during the mid-cretaceous. *Paleoceanography* 17. <https://doi.org/10.1029/2001PA000623>.
- Lehmann, B., 2022. Early Cambrian Highly Metalliferous Black Shale in South China: Cu and Zn Isotopes and a Short Review of Other Non-traditional Stable Isotopes. *Mineral. Deposita* 57, 1167–1187. <https://doi.org/10.1007/s00126-022-01097-0>.
- Li, Y., Fan, T., Zhang, Jinchuan, Zhang, Junpeng, Wei, X., Hu, X., Zeng, W., Fu, W., 2015. Geochemical changes in the early Cambrian interval of the Yangtze Platform, South China: Implications for hydrothermal influences and paleocean redox conditions. *J. Asian Earth Sci.* 109, 100–123. <https://doi.org/10.1016/j.jseas.2015.05.003>.
- Li, C., Zhang, Z., Jin, C., Cheng, M., Wang, H., Huang, J., Algeo, T.J., 2020. Spatiotemporal evolution and causes of marine euxinia in the early Cambrian Nanhu Basin (South China). *Palaeogeogr. Palaeoclimatol. Palaeoecol.* 546, 109676. <https://doi.org/10.1016/j.palaeo.2020.109676>.
- Li, Chenqing, Dong, L., Ma, H., Liu, H., Li, Chao, Pei, H., Shen, B., 2022a. Formation of the massive bedded chert and coupled Silicon and Iron cycles during the Ediacaran-Cambrian transition. *Earth Planet. Sci. Lett.* 594, 117721. <https://doi.org/10.1016/j.epsl.2022.117721>.
- Li, Y., Liu, G., Song, Z., Zhang, B., Sun, M., Tian, X., Yang, D., Wang, Y., Zhu, L., Cao, Y., 2022b. Organic matter enrichment due to high primary productivity in the deep-water shelf: Insights from the lower Cambrian Qiongzhusi shales of the Central Sichuan Basin, SW China. *J. Asian Earth Sci.* 239, 105417. <https://doi.org/10.1016/j.jseas.2022.105417>.
- Li, W., Liu, C., Brantley, S.L., Xu, Z., Zhao, T., Liu, T., Yu, C., Xue, D., Zhao, Z., Cui, L., Zhang, Z., Fan, B., Gu, X., 2016. Deep weathering along a granite ridgeline in a subtropical climate. *Chem. Geol.* 427, 17–34. <https://doi.org/10.1016/j.chemgeo.2016.02.014>.
- Li, Z., Algeo, T.J., Guo, X., Fan, J., Du, X., Lu, Y., 2017. Paleo-environmental cyclicity in the early Silurian Yangtze Sea (South China): Tectonic or glacio-eustatic control? *Palaeogeogr. Palaeoclimatol. Palaeoecol.* 466, 59–76. <https://doi.org/10.1016/j.palaeo.2016.11.007>.
- Liu, J., Ding, W., Wang, R., Wu, Z., Gong, D., Wang, X., Yin, S., Jiao, B., 2018. Quartz types in shale and their effect on geomechanical properties: an example from the lower Cambrian Niutitang Formation in the Cen'gong block, South China. *Appl. Clay Sci.* 163, 100–107. <https://doi.org/10.1016/j.clay.2018.07.019>.
- Liu, Q., Li, P., Jin, Z., Liang, X., Zhu, D., Wu, X., Meng, Q., Liu, J., Fu, Q., Zhao, J., 2021. Preservation of organic matter in shale linked to bacterial sulfate reduction (BSR) and volcanic activity under marine and lacustrine depositional environments. *Mar. Pet. Geol.* 127, 104950. <https://doi.org/10.1016/j.marpetgeo.2021.104950>.
- Liu, Y.-X., Li, Y.-G., Lu, Z.-T., Zhang, J.-W., Han, T., 2023. The mechanism of zinc enrichment in the lower Cambrian black shale in South China. *Acta Mineral. Sin.* 43, 481–489. <https://doi.org/10.16461/j.cnki.1000-4734.2023.43.029> (in Chinese with English abstract).
- Lyons, T.W., Reinhard, C.T., Planavsky, N.J., 2014. The rise of oxygen in Earth's early ocean and atmosphere. *Nature* 506, 307–315. <https://doi.org/10.1038/nature13068>.
- Maliva, R.G., Knoll, A.H., Simonson, B.M., 2005. Secular change in the Precambrian silica cycle: Insights from chert petrology. *Geol. Soc. Am. Bull.* 117, 835. <https://doi.org/10.1130/b25555.1>.
- Marchig, V., Gundlach, H., Möller, P., Schley, F., 1982. Some geochemical indicators for discrimination between diagenetic and hydrothermal metalliferous sediments. *Mar. Geol.* 50, 241–256. [https://doi.org/10.1016/0025-3227\(82\)90141-4](https://doi.org/10.1016/0025-3227(82)90141-4).
- Marin-Carbonne, J., Robert, F., Chaussidon, M., 2014. The silicon and oxygen isotope compositions of Precambrian cherts: a record of oceanic paleo-temperatures? *Precambrian Res.* 247, 223–234. <https://doi.org/10.1016/j.precamres.2014.03.016>.
- McLennan, S.M., 1989. Rare earth elements in sedimentary rocks: influence of provenance and sedimentary processes. *Rev. Mineral. Geochem.* 21, 169–200.
- McLennan, S.M., 1993. Weathering and Global Denudation. *J. Geol.* 101, 295–303. <https://doi.org/10.1086/648222>.
- McLennan, S.M., Hemming, S., McDaniel, D.K., Hanson, G.N., 1993. Geochemical approaches to sedimentation, provenance, and tectonics. In: Geological Society of America Special Papers. Geological Society of America, pp. 21–40. <https://doi.org/10.1130/SPE284-p21>.
- Merdith, A.S., Williams, S.E., Collins, A.S., Tetley, M.G., Mulder, J.A., Blades, M.L., Young, A., Armistead, S.E., Cannon, J., Zahirovic, S., Müller, R.D., 2021. Extending full-plate tectonic models into deep time: linking the Neoproterozoic and the Phanerozoic. *Earth Sci. Rev.* 214, 103477. <https://doi.org/10.1016/j.earscirev.2020.103477>.
- Migdisov, A., Williams-Jones, A.E., Brugger, J., Caporuscio, F.A., 2016. Hydrothermal transport, deposition, and fractionation of the REE: Experimental data and thermodynamic calculations. *Chem. Geol.* 439, 13–42. <https://doi.org/10.1016/j.chemgeo.2016.06.005>.
- Mort, H., Jacquot, O., Adatte, T., Steinmann, P., Föllmi, K., Matera, V., Berner, Z., Stüben, D., 2007. The Cenomanian/Turonian anoxic event at the Bonarelli Level in Italy and Spain: enhanced productivity and/or better preservation? *Cretac. Res.* 28, 597–612. <https://doi.org/10.1016/j.cretres.2006.09.003>.
- Nesbitt, H.W., Young, G.M., 1982. Early Proterozoic climates and plate motions inferred from major element chemistry of lutesites. *Nature* 299, 715–717. <https://doi.org/10.1038/299715a0>.
- Ouyang, S., Ji, J., Li, C., Mills, B.J.W., Wei, G., Hedding, D.W., Li, G., 2025. Phanerozoic Onset of massive Continental Weathering. *Geophys. Res. Lett.* 52. <https://doi.org/10.1029/2025GL117072> e2025GL117072.
- Panahi, A., Young, G.M., Rainbird, R.H., 2000. Behavior of major and trace elements (including REE) during Paleoproterozoic pedogenesis and diagenetic alteration of an Archean granite near Ville Marie, Québec, Canada. *Geochim. Cosmochim. Acta* 64, 2199–2220. [https://doi.org/10.1016/S0016-7037\(99\)00420-2](https://doi.org/10.1016/S0016-7037(99)00420-2).
- Pi, D.-H., Liu, C.-Q., Shields-Zhou, G.A., Jiang, S.-Y., 2013. Trace and rare earth element geochemistry of black shale and kerogen in the early Cambrian Niutitang Formation in Guizhou province, South China: Constraints for redox environments and origin of metal enrichments. *Precambrian Res.* 225, 218–229. <https://doi.org/10.1016/j.precamres.2011.07.004>.
- Piper, D.Z., Perkins, R.B., 2004. A modern vs. Permian black shale—the hydrography, primary productivity, and water-column chemistry of deposition. *Chem. Geol.* 206, 177–197. <https://doi.org/10.1016/j.chemgeo.2003.12.006>.
- Pohl, C., Löffler, A., Hennings, U., 2004. A sediment trap flux study for trace metals under seasonal aspects in the stratified Baltic Sea (Gotland Basin; 57°19.20'N; 20°03.00'E). *Mar. Chem.* 84, 143–160. <https://doi.org/10.1016/j.jmarsci.2003.07.002>.
- Rasmussen, B., Muhling, J.R., 2021. Development of a greenalite-silica shuttle during incursions of hydrothermal vent plumes onto Neoarchean shelf, Hamersley region, Australia. *Precambrian Res.* 353, 106003. <https://doi.org/10.1016/j.precamres.2020.106003>.
- Rasmussen, B., Muhling, J.R., Suvorova, A., Krapež, B., 2017. Greenalite precipitation linked to the deposition of banded iron formations downslope from a late Archean carbonate platform. *Precambrian Res.* 290, 49–62. <https://doi.org/10.1016/j.precamres.2016.12.005>.
- Reddy, T.R., Zheng, X.-Y., Roden, E.E., Beard, B.L., Johnson, C.M., 2016. Silicon isotope fractionation during microbial reduction of Fe (III)-Si gels under Archean seawater conditions and implications for iron formation genesis. *Geochim. Cosmochim. Acta* 190, 85–99. <https://doi.org/10.1016/j.gca.2016.06.035>.
- Ribouleau, A., Baudin, F., Deconinck, J.-F., Derenne, S., Largeau, C., Tribouillard, N., 2003. Depositional conditions and organic matter preservation pathways in an epicontinent environment: the Upper Jurassic Kashir Oil Shales (Volga Basin, Russia). *Palaeogeogr. Palaeoclimatol. Palaeoecol.* 197, 171–197. [https://doi.org/10.1016/s0031-0182\(03\)00460-7](https://doi.org/10.1016/s0031-0182(03)00460-7).

- Shao, J., Yang, S., 2012. Does chemical index of alteration (CIA) reflect silicate weathering and monsoonal climate in the Changjiang River basin? *Chin. Sci. Bull.* 57, 1178–1187. <https://doi.org/10.1007/s11434-011-4954-5>.
- Siever, R., 1992. The silica cycle in the Precambrian. *Geochim. Cosmochim. Acta* 56, 3265–3272. [https://doi.org/10.1016/0016-7037\(92\)90303-Z](https://doi.org/10.1016/0016-7037(92)90303-Z).
- Steiner, M., Wallis, E., Erdtmann, B.-D., Zhao, Y., Yang, R., 2001. Submarine-hydrothermal exhalative ore layers in black shales from South China and associated fossils D insights into a lower Cambrian facies and bio-evolution. *Palaeogeogr. Palaeoclimatol. Palaeoecol.* 169, 165–191. [https://doi.org/10.1016/S0031-0182\(01\)00208-5](https://doi.org/10.1016/S0031-0182(01)00208-5).
- Steiner, M., Li, G., Qian, Y., Zhu, M., Erdtmann, B.-D., 2007. Neoproterozoic to early Cambrian small shelly fossil assemblages and a revised biostratigraphic correlation of the Yangtze Platform (China). *Palaeogeogr. Palaeoclimatol. Palaeoecol.* 254, 67–99. <https://doi.org/10.1016/j.palaeo.2007.03.046>.
- Tatzel, M., Von Blanckenburg, F., Oelze, M., Bouchez, J., Hipppler, D., 2017. Late Neoproterozoic seawater oxygenation by siliceous sponges. *Nat. Commun.* 8. <https://doi.org/10.1038/s41467-017-00586-5>.
- Taylor, S.R., McLennan, S.M., 1985. *The Continental Crust: Its Composition and Evolution*. Blackwell scientific publication, Oxford.
- Tostevin, R., Sevign, S., 2024. The role of Fe (II)-silicate gel in the generation of Archean and Paleoproterozoic chert. *Geology* 52, 706–711. <https://doi.org/10.1130/G52202.1>.
- Trégouer, P.J., Sutton, J.N., Brzezinski, M., Charette, M.A., Devries, T., Dutkiewicz, S., Ehler, C., Hawkings, J., Leynaert, A., Liu, S.M., Llopis Monferrer, N., López-Acosta, M., Maldonado, M., Rahman, S., Ran, L., Rouxel, O., 2021. Reviews and syntheses: the biogeochemical cycle of silicon in the modern ocean. *Biogeosciences* 18, 1269–1289. <https://doi.org/10.5194/bg-18-1269-2021>.
- Tribouillard, N., Algeo, T.J., Lyons, T., Riboulleau, A., 2006. Trace metals as paleoredox and paleoproductivity proxies: an update. *Chem. Geol.* 232, 12–32. <https://doi.org/10.1016/j.chemgeo.2006.02.012>.
- Tribouillard, N., Algeo, T.J., Baudin, F., Riboulleau, A., 2012. Analysis of marine environmental conditions based on molybdenum–uranium covariation—applications to Mesozoic paleoceanography. *Chem. Geol.* 324–325, 46–58. <https://doi.org/10.1016/j.chemgeo.2011.09.009>.
- Van Der Weijden, C.H., 2002. Pitfalls of normalization of marine geochemical data using a common divisor. *Mar. Geol.* 184, 167–187. [https://doi.org/10.1016/S0025-3227\(01\)00297-3](https://doi.org/10.1016/S0025-3227(01)00297-3).
- Vevers, J.J., Walter, M.R., Scheibner, E., 1997. Neoproterozoic Tectonics of Australia–Antarctica and Laurentia and the 560 Ma Birth of the Pacific Ocean Reflect the 400 M.Y. Pangean Supercycle. *J. Geol.* 105, 225–242. <https://doi.org/10.1086/515914>.
- Von Eynatten, H., Tolosana-Delgado, R., Karius, V., 2012. Sediment generation in modern glacial settings: Grain-size and source-rock control on sediment composition. *Sediment. Geol.* 280, 80–92. <https://doi.org/10.1016/j.sedgeo.2012.03.008>.
- Wang, J., 2003. History of Neoproterozoic rift basins in South China: implications for Rodinia break-up. *Precambrian Res.* 122, 141–158. [https://doi.org/10.1016/S0301-9268\(02\)00209-7](https://doi.org/10.1016/S0301-9268(02)00209-7).
- Wang, H., Chu, X., Liu, B., Hou, H., Ma, L., 1985. *Atlas of the Paleogeography of China. Sinomap press, Beijing*.
- Wang, Y., Xu, H., Merino, E., Konishi, H., 2009. Generation of banded iron formations by internal dynamics and leaching of oceanic crust. *Nat. Geosci.* 2, 781–784. <https://doi.org/10.1038/ngeo652>.
- Wang, H., Li, Z., Liu, S., Ran, B., Song, J., Li, J., Ye, Y., Li, N., 2020. Ediacaran extension along the northern margin of the Yangtze Platform, South China: Constraints from the lithofacies and geochemistry of the Doushantuo Formation. *Mar. Pet. Geol.* 112, 104056. <https://doi.org/10.1016/j.marpgeo.2019.104056>.
- Wei, X., Gao, B., Zhang, H., Wu, A., Zhang, X., 1984. *Regional Geology of Jiangxi Province. Geology Press, Beijing*.
- White, A.F., Bullen, T.D., Schulz, M.S., Blum, A.E., Huntington, T.G., Peters, N.E., 2001. Differential rates of feldspar weathering in granitic regoliths. *Geochim. Cosmochim. Acta* 65, 847–869. [https://doi.org/10.1016/s0016-7037\(00\)00577-9](https://doi.org/10.1016/s0016-7037(00)00577-9).
- Wu, C.D., 2000. Restoration of ancient marine environment during the Sinian-Cambrian alternation in western Hunan. *Earth Science Frontiers.* 45–57 (in Chinese with English abstract).
- Wu, Y., Tian, H., Gong, D., Li, T., Zhou, Q., 2020a. Paleo-environmental variation and its control on organic matter enrichment of black shales from shallow shelf to slope regions on the Upper Yangtze Platform during Cambrian Stage 3. *Palaeogeogr.* *Palaeoclimatol. Palaeoecol.* 545, 109653. <https://doi.org/10.1016/j.palaeo.2020.109653>.
- Wu, Y., Tian, H., Gong, D., Li, T., Zhou, Q., 2020b. Paleo-environmental variation and its control on organic matter enrichment of black shales from shallow shelf to slope regions on the Upper Yangtze Platform during Cambrian Stage 3. *Palaeogeogr. Palaeoclimatol. Palaeoecol.* 545, 109653. <https://doi.org/10.1016/j.palaeo.2020.109653>.
- Xi, Z., Tang, S., Zhang, S., Yi, Y., Fang, F., Ye, Y., 2019. Characterization of quartz in the Wufeng Formation in Northwest Hunan Province, South China and its implications for reservoir quality. *J. Pet. Sci. Eng.* 179, 979–996. <https://doi.org/10.1016/j.petrol.2019.04.051>.
- Xie, X., Zhu, G., Wang, Y., 2021. The Influence of Syngenetic Hydrothermal Silica Fluid on Organic Matter Preservation in Lower Cambrian Niutitang Formation, South China. *Mar. Pet. Geol.* 129, 105098. <https://doi.org/10.1016/j.marpetgeo.2021.105098>.
- Yang, Z.J., 1981. Discussion on 'Jiangnan deep fault'. *East China Geol.* 28–38 (in Chinese with English abstract).
- Zeng, W., Zhang, J., Ding, W., Zhao, S., Zhang, Y., Liu, Z., Jiu, K., 2013. Fracture development in Paleozoic shale of Chongqing area (South China). Part one: Fracture characteristics and comparative analysis of main controlling factors. *J. Asian Earth Sci.* 75, 251–266. <https://doi.org/10.1016/j.jseas.2013.07.014>.
- Zhai, L., Wu, C., Ye, Y., Zhang, S., Wang, Y., 2018. Fluctuations in chemical weathering on the Yangtze Block during the Ediacaran–Cambrian transition: Implications for paleoclimatic conditions and the marine carbon cycle. *Palaeogeogr. Palaeoclimatol. Palaeoecol.* 490, 280–292. <https://doi.org/10.1016/j.palaeo.2017.11.006>.
- Zhang, K., Jiang, Z., Yin, L., Gao, Z., Wang, P., Song, Y., Jia, C., Liu, W., Liu, T., Xie, X., Li, Y., 2017. Controlling functions of hydrothermal activity to shale gas content-taking lower Cambrian in Xiuwu Basin as an example. *Mar. Pet. Geol.* 85, 177–193. <https://doi.org/10.1016/j.marpetgeo.2017.05.012>.
- Zhang, K., Li, Z., Jiang, S., Jiang, Z., Wen, M., Jia, C., Song, Y., Liu, W., Huang, Y., Xie, X., Liu, T., Wang, P., Shan, C., Wu, Y., 2018. Comparative analysis of the siliceous source and organic matter enrichment mechanism of the Upper Ordovician–Lower Silurian Shale in the Upper-Lower Yangtze Area. *Minerals* 8, 283. <https://doi.org/10.3390/min8070283>.
- Zhang, G., Chen, D., Huang, K.-J., Liu, M., Huang, T., Yeasmin, R., Fu, Y., 2021. Dramatic attenuation of continental weathering during the Ediacaran–Cambrian transition: Implications for the climatic-oceanic-biological co-evolution. *Glob. Planet. Chang.* 203, 103518. <https://doi.org/10.1016/j.gloplacha.2021.103518>.
- Zhang, G., Chen, X., Wang, B., Zhang, B., Chen, L., 2022a. Geochemical characteristics of black rock series in the transition zone between Sinian and Cambrian Systems in the Xuefengshan area: implications for their provenances, paleoclimate and tectonic setting. *Bull. Mineral. Petro. Geochim.* 41, 414–428. <https://doi.org/10.19658/j.issn.1007-2802.2022.41.007> (in Chinese with English abstract).
- Zhang, J., Shi, M., Wang, D., Tong, Z., Hou, X., Niu, J., Li, X., Li, Z., Zhang, P., Huang, Y., 2022b. Fields and directions for shale gas exploration in China. *Nat. Gas Ind.* B 9, 20–32. <https://doi.org/10.1016/j.ngib.2021.08.014>.
- Zhang, Y., Huang, D., Zhang, L., Wan, C., Luo, H., Shao, D., Meng, K., Yan, J., Zhang, T., 2023. Characteristics of biogenic silica in Cambrian Shuijingtuo Formation shale and its influence on shale gas enrichment in Yichang area, western Hubei Province. *Earth Science Frontiers.* 30, 83–100. <https://doi.org/10.13745/j.esf.sf.2022.5.40> (in Chinese with English abstract).
- Zheng, Y.-F., Wu, R.-X., Wu, Y.-B., Zhang, S.-B., Yuan, H., Wu, F.-Y., 2008. Rift melting of juvenile arc-derived crust: Geochemical evidence from Neoproterozoic volcanic and granitic rocks in the Jiangnan Orogen. *South China. Precambrian Res.* 163, 351–383. <https://doi.org/10.1016/j.precamres.2008.01.004>.
- Zheng, X.-Y., Beard, B.L., Reddy, T.R., Roden, E.E., Johnson, C.M., 2016. Abiologic silicon isotope fractionation between aqueous Si and Fe (III)-Si gel in simulated Archean seawater: Implications for Si isotope records in Precambrian sedimentary rocks. *Geochim. Cosmochim. Acta* 187, 102–122. <https://doi.org/10.1016/j.gca.2016.05.012>.
- Zhou, D., Dong, H., Huang, X., Liang, Y., Deng, Z., Huang, L., Jiang, S., 2024. The paleoceanic environment and organic matter enrichment mechanism of the early Cambrian in the southern lower Yangtze Platform China. *Mar. Pet. Geol.* 107119. <https://doi.org/10.1016/j.marpgeo.2024.107119>.
- Zhu, G., Zhao, K., Li, T., Zhang, Z., Tang, S., Wang, P., 2021. Anomalously high enrichment of mercury in early Cambrian black shales in South China. *J. Asian Earth Sci.* 216, 104794. <https://doi.org/10.1016/j.jseas.2021.104794>.